

# The crucial role of adhesion in the transmigration of active droplets through interstitial orifices

A. Tiribocchi\*,<sup>1</sup> M. Durve,<sup>2</sup> M. Lauricella,<sup>3</sup> A. Montessori,<sup>4</sup> D. Marenduzzo,<sup>5</sup> and S. Succi<sup>2,3,6</sup>

<sup>1</sup>*Istituto per le Applicazioni del Calcolo CNR, via dei Taurini 19, 00185 Rome, Italy*  
*a.tiribocchi@iac.cnr.it*

<sup>2</sup>*Center for Life Nano Science@La Sapienza, Istituto Italiano di Tecnologia, 00161 Roma, Italy*

<sup>3</sup>*Istituto per le Applicazioni del Calcolo CNR, via dei Taurini 19, 00185 Rome, Italy*

<sup>4</sup>*Department of Engineering, Roma Tre University, Via Vito Volterra 62, 00146 Rome, Italy*

<sup>5</sup>*Scottish Universities Physics Alliance, School of Physics and Astronomy,  
University of Edinburgh, Edinburgh EH9 3JZ, United Kingdom*

<sup>6</sup>*Department of Physics, Harvard University, Cambridge, MA, 02138, USA*

## ABSTRACT

Active fluid droplets are a class of soft materials exhibiting autonomous motion sustained by an energy supply. Such systems have been shown to capture motility regimes typical of biological cells and are ideal candidates as building-block for the fabrication of soft biomimetic materials of interest in pharmacology, tissue engineering and lab on chip devices. While their behavior is well established in unconstrained environments, much less is known about their dynamics under strong confinement. Here, we numerically study the physics of a droplet of active polar fluid migrating within a microchannel hosting a constriction with adhesive properties, and report evidence of a striking variety of dynamic regimes and morphological features, whose properties crucially depend upon droplet speed and elasticity, degree of confinement within the constriction and adhesiveness to the pore. Our results suggest that non-uniform adhesion forces are instrumental in enabling the crossing through narrow orifices, in contrast to larger gaps where a careful balance between speed and elasticity is sufficient to guarantee the transition. These observations may be useful for improving the design of artificial micro-swimmers, of interest in material science and pharmaceuticals, and potentially for cell sorting in microfluidic devices.

## INTRODUCTION

Over the last decades, much research has been addressed to active matter, an area of physics concerning systems whose internal constituents are capable of converting energy, adsorbed from the surrounding environment, into work or systematic movement [1, 2]. A particular class of such systems is represented by active gels, densely packed soft materials in which the internal constituents have the tendency to assemble and align, producing structures with polar or nematic order [3–7]. Examples abound in biology, ranging from bacterial colonies [8–10] to actin filaments and microtubule bundles powered by motor proteins [11–14]. Such materials can be further divided in two broad classes, depending upon the structure of the fluid flow generated in their surroundings. In contractile materials the fluid is pulled inward axially and emitted equatorially, while in extensile ones the opposite holds [1]. Their inherent non-equilibrium nature fosters a wealth of sought-after phenomena with spectacular mesoscale collective behaviors, including spontaneous flows [12, 15, 16], turbulent-like motion in fluids with low Reynolds numbers [17] and unexpected rheological properties [18, 19], to name but a few.

Of particular relevance to us are active fluid droplets, bio-inspired self-propelled emulsions whose autonomous motion is driven by a hierarchically-assembled active gel located within (either uniformly [20–22] or confined in

a shell [23, 24]) or adsorbed onto the interface [12]. Although distant from living cells, these droplets have been shown capable of capturing a number of features typical of cell dynamics, such as swimming [20], crawling [25], and spontaneous division [21], and have also served as a model tool for studying collective cell migration [26] and extrusion process in epithelial tissues [27]. Alongside their ability in describing the functioning of such complex biological processes, they could also offer a powerful platform for the design of programmable biomimetic soft materials [12, 28] with enhanced mechanical properties, such as a higher control over direction of motion and persistent motility, if compared to their passive analogues. These materials may be useful in a number of technological applications ranging from pharmaceuticals, as microscopic cargoes for the transport and release of drugs toward a diseased tissue [29], and food science, as carriers for the targeted delivery of the nutrients encapsulated within [30], to material science for the design of engineered tissues [27].

In such circumstances, as well as under many physiologically-relevant conditions (such as within capillary vessels [31]), a droplet often migrates through pore-sized constrictions, whose diameter is typically much narrower than that of the drop itself (of the order of tens of micrometers). From a fluid dynamics perspective, the crossing through interstices poses additional challenges with respect to a motion occurring in an unconstrained environment. In a purely passive system, the scenario

is well established [32, 33]. A Newtonian fluid droplet placed in an external flow would undergo deformations governed by the interplay between hydrodynamic interactions, favouring shape changes, and capillary forces, which oppose morphological modifications and tend to hold a spherical geometry. Their balance is controlled by the capillary number  $Ca = \eta v / \sigma$ , where  $v$  is the droplet speed,  $\sigma$  its surface tension  $\eta$  the shear viscosity. An intense driving flow, for example, may favour the crossing through the pore if properly counterbalanced by a sufficiently high surface tension, which would guarantee the stability of the drop and avoid its rupture.

The inclusion of an active gel could substantially change this picture. A non-homogeneous distribution of such material onto the fluid interface, for example, besides fostering the formation of coherent spontaneous flows [12], may concurrently alter the surface tension of the drop, thus considerably impacting on morphology and mechanics when moving in a confined environment. If the active gel is encapsulated within, the drop is expected to harden, thus further opposing deformations. In addition, assembly and arrangement of the active material could decisively affect the elasticity of the drop and the structure of the fluid flow [20, 25], hence imposing further constraints on the ability to migrate across a constriction.

Understanding their dynamics as well as their fluid-structure interactions, especially under controlled experimental conditions mimicking realistic environments, is thus essential for an optimal manufacturing of these materials. To make progress along this direction, the building of reliable computational models is often mandatory due to the complicated structure of the equations governing their physics [1, 4, 34]. Well-established numerical approaches (such as phase-field methods [35–37] and lattice Boltzmann algorithms [20, 25, 38, 39]) combined with continuum theories have provided a robust machinery to model the dynamics of active gel droplets in pore-free geometries [20, 26, 40–43]. However, their motion through narrow interstices has not been sufficiently investigated so far.

In this paper, we numerically study the transmigration of a droplet of active polar fluid across a constriction, following a design inspired to a typical lab-on-chip microfluidic device [44–46]. This one is modeled as a long thin channel hosting a pore-like interstice made of two solid pillars glued to opposite flat walls. The theoretical framework to investigate the physics of the transmigration is based on a phase-field-like approach, whose details are illustrated in the section Methods. It basically consists of a set of phase fields  $\phi_i(\mathbf{r}, t)$  ( $i = 1, 2, 3$ ), where  $\phi_1(\mathbf{r}, t)$  accounts for the density of the active material encapsulated within our active droplet, while  $\phi_2(\mathbf{r})$  and  $\phi_3(\mathbf{r})$  are two *static* fluid-free fields modeling the pillars of the constriction [42]. The active material is a contractile gel whose mesoscopic orientational order is captured by a

liquid crystal vector field  $\mathbf{P}(\mathbf{r}, t)$ , while the global fluid velocity is represented by a further vector field  $\mathbf{v}(\mathbf{r}, t)$ . The dynamics of  $\phi_1$  and  $\mathbf{P}(\mathbf{r}, t)$  are governed by advection-relaxation equations while that of the fluid velocity  $\mathbf{v}(\mathbf{r}, t)$  obeys the Navier-Stokes equation [47]. The equilibrium properties of this system are described by a Landau-de Gennes free-energy functional [48], augmented with a repulsive term between droplet and pillars plus a contribution favouring adhesion between the fluid interface and the pore.

Extensive lattice Boltzmann simulations show a rich variety of dynamic regimes whose physics is controlled by i) ratio between size of the constriction and droplet diameter, ii) speed and elasticity (including interfacial tension and polar field deformations) of the droplet and iii) adhesiveness between pillars of the pore and droplet itself. Central to these results is that such adhesion forces are decisive to enable the transmigration, especially for narrow interstices. Indeed our findings support the view that, while for wide pores the crossing is guaranteed by a careful balance between droplet speed and elasticity, for smaller ones it is generally forbidden unless adhesion forces come into play, provided that at the pore entry they are higher than at the exit. Within the orifice, the droplet is found to display a series of shape deformations (from ampule-like to hourglass geometries) whose stability is controlled by the interplay between fluid velocity, exhibiting short-lived rectilinear flow, and elasticity of fluid interface and contractile gel, hosting splay and bend liquid crystal distortions. The minimal design of our computational model might suggest that the functioning of biomimetic droplet-based materials could rely exclusively upon a mesoscale physics-based machinery rather than on complex microscopic multi-body interactions governing the physics at lower lengthscales.

## RESULTS

### Motile droplet within a microfluidic channel

The mechanism leading to the self-propulsion of a droplet comprising a contractile material, such as a network of actin filaments cross-linked with myosin proteins, has been theoretically investigated in previous works [20, 21, 25, 35, 36, 40, 43, 49]. Following Refs.[20, 25], we consider a 2D mixture in which the active material is described in terms of a liquid crystal whose mean orientation is captured by a polar field while the contractile effect is modeled, at a mesoscale level, via a stress term (see the section Methods for further details). This one takes the form  $\sigma_{\alpha\beta}^{\text{active}} \sim -\zeta \phi_1 P_\alpha P_\beta$ , which is invariant under global polarity inversion and whose strength is gauged by the activity  $\zeta$ , negative for contractile mixtures. If  $\zeta$  exceeds a threshold value, the active stress causes a spontaneous flow which breaks the inversion symmetry

and sets the droplet into motion, along a direction controlled by an emerging splay deformation.

The essential steps of such dynamics are shown in Fig.1. The droplet is placed within a microfluidic channel and is initialized as a circular region where  $\phi_1 = \phi_0$  inside and  $\phi_1 = 0$  outside (Fig.1a). The polar field is initially uniform and aligned along the  $y$  direction within the droplet (no anchoring of the polarization is set at the droplet interface), while it is zero outside. This means that the contractile gel is confined within the active drop and is polarized, while the surrounding region represents an isotropic Newtonian fluid. The activity  $\zeta$  is then turned on and is set at a value allowing for the motion of the droplet. Before attaining a motile state, the drop temporarily elongates perpendicularly to the polarization  $\mathbf{P}$  remaining motionless, an effect caused by the competition between interfacial tension, opposing shape deformations, and contractile stress, favouring hydrodynamic instability (see Fig.1b). In this condition, the fluid flow surrounding the droplet acquires a four-roll structure (it is pulled inward equatorially and emitted axially, see Fig.1f), thus preventing any net motion. Such an arrangement essentially results from the sum of the dipolar hydrodynamic flows formed around each contractile unit (such as the actomyosin complex, Fig.1d). Indeed, at the microscopic level, the motor protein would pull two protein filaments together (Fig.1e), causing an inward force pair that produces a contractile stress (see also the section Methods). This process also modifies the direction of the polarization, which remains basically uniform in the bulk but slightly deforms near the droplet interface, where a preferential perpendicular orientation emerges almost everywhere except at the ends of the elongated drop. The active anchoring, genuinely induced by the contractile stress [50], will persist in the following motile state, although its orientation will be considerably affected by the confinement conditions (especially when the drop migrates through narrow interstices, see the next sections).

Afterwards, the non-motile configuration becomes unstable with respect to splay distortions, since the contractile stress is high enough to overcome the resistance to deformation mediated by the elastic constant  $\kappa$ . A suitable dimensionless quantity controlling the balance between activity and elasticity is the Ericksen number  $Er = \zeta R^2 / \kappa$  ( $R$  is the droplet radius) which ranges approximately from 5 to 50 in our simulations (see Supplementary Note 1 and 2 for details on parameter values), thus high enough to destabilize the droplet and lead to its motion. The vectors of  $\mathbf{P}$  then fan outwards arranging into a typical liquid crystal splay deformation (where  $\nabla \cdot \mathbf{P} > 0$ ), while the droplet starts to move along the direction set by  $\mathbf{P}$  (see Fig.1c) sustained by two symmetric counter-rotating vortices (see Fig.1g) [20]. This motion would last over long periods of time and would proceed unidirectionally with a steady velocity, typical of an ac-

tive droplet swimming in a Newtonian fluid in the absence of external perturbations or constraints. We note that such spontaneous motion has been found to partially model the dynamics of tumour cells moving inside an elastic gel [20, 51], where self-motility is solely triggered by myosin contractility rather than other mechanisms such as actin polymerization, usually essential in crawling cells [52].

The picture described so far dramatically changes when a droplet migrates in a complex environment flowing, for example, across a constriction of size much narrower than that of the droplet itself. In the next section we precisely investigate this process providing an accurate description of the fluid-structure interaction along with a minimal set of key physical ingredients controlling the transmigration.

### Motile droplet across a wide constriction

We start off by considering the migration across a constriction of size  $h$  comparable with the diameter  $D$  of the active droplet. In Fig.2a-f (and Supplementary Movie 1) we show a time sequence of such process for  $\lambda = h/D \simeq 0.8$ , where  $\lambda$  is the confinement parameter. The droplet is initialized as in the pore-free case, i.e. a circular region where the polarization is initially parallel to  $y$ -direction. Once the activity is turned on ( $\zeta = -8 \times 10^{-4}$ ), the droplet elongates in the direction perpendicular to  $\mathbf{P}$  and then acquires a unidirectional motion at constant velocity (Fig.2a and Fig.3a,d, where position and speed of the center of mass are plotted), a process akin to that described in the previous paragraph. In the vicinity of the pore (modeled placing two solid pillars at distance  $h$ , see the Methods), it slightly squeezes and stretches forward (Fig.2b), while its speed gradually diminishes up to a minimum value, attained approximately once the leading edge enters the gap (Fig.3g,h). However, this slowdown does not arrest the motion, which proceeds favoured by a series of weak morphological deformations sufficient to boost the droplet and guarantee the transmigration. Within the orifice, the droplet undergoes a light longitudinal stretching and compression (Fig.2c) fostering an increase of speed of approximately three times higher than the value at the entrance of the pore (Fig.3i), followed by a mild decompression (Fig.2d) where the speed goes back to its steady unconstrained value (Fig.3j). Afterwards, the droplet expands (Fig.2e) restoring the typical crescent-like shape (Fig.2f) observed out of the pore. During the process, the polarization remains basically unaltered, preserving its splay arrangement kept for the entire course of the migration.

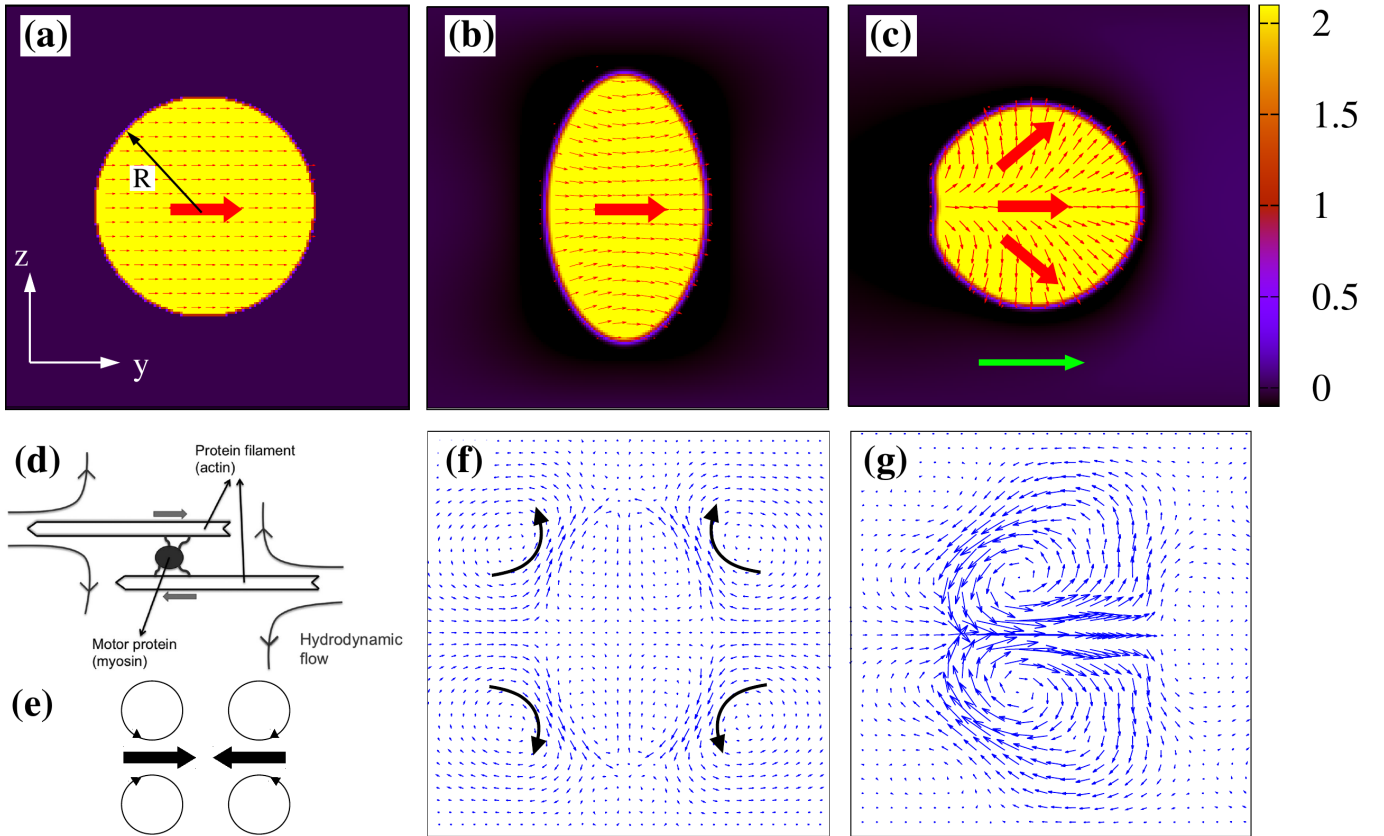


Figure 1. **Shapes and velocity field of a motile contractile droplet.** (a) Initial configuration of an active droplet. The red arrows indicate the direction of the polarization field  $\mathbf{P}$ . The droplet is placed within a microfluidic channel of size  $L_y = 500$  and  $L_z = 170$ . Here only a portion of the lattice is shown. (b) Intermediate pre-motile state of the contractile suspension with  $\zeta = -8 \times 10^{-4}$ . The droplet elongates perpendicularly to the direction of the polarization which remains essentially parallel to the  $y$  direction. (c) However, this value of  $\zeta$  is sufficiently high to destabilize the polarization, which gives rise to a large splay deformation. Once this occurs, the drop acquires a unidirectional motion along the direction indicated by the green arrow. (d) Schematic view of the hydrodynamic flow produced by a contractile material, such as the actomyosin. The myosin protein pulls two actin filaments along opposite directions (indicated by tick grey arrows), yielding a four-roll flow in their surroundings. Panel (d) is adapted from E. Tjhung, D. Marenduzzo, and M. E. Cates, “Spontaneous symmetry breaking in active droplets provides a generic route to motility”, *Proc. Nat. Acad. Sci. USA* **109**, 12381-12386 (2012). (e) A minimal model of the force dipole produced by a contractile material. The thick black arrows indicate the direction of the force dipole while the circles represent the emerging four vortices of fluid. (f)-(g) Velocity field of the pre-motile (b) and motile (c) states. In the former, the fluid is pulled inward along the equator (parallel to the direction of  $\mathbf{P}$ ) and emitted axially (perpendicularly to  $\mathbf{P}$ ), giving rise to a macroscopic four-vortex structure. In the latter, a splay distortion fosters the formation of two counter-rotating vortices pushing the drop forward. The droplet radius at equilibrium is  $R = 45$  lattice sites and the color map represents the value of the order parameter  $\phi_1$ , ranging between 0 (black) and 2 (yellow).

### Motile droplet across a medium size constriction

Decreasing  $\lambda$  enough can permanently hinder the crossing through the pore. This is shown in Supplementary Movie 2 where we simulate the dynamics of an active droplet swimming within a microchannel with  $\lambda \simeq 0.5$ . The droplet initially self-propels forward following the mechanism previously described and, once near the pore, hits the pillars, which halt its motions impeding the transmigration. Note that, despite the stop, the droplet partially preserves a crescent-like shape, due to the permanent splay distortion of the liquid crystal caused by the contractile activity.

These results do not automatically rule out the possibility to observe a crossing, an event which may occur, for example, if the activity  $|\zeta|$  is higher and the surface tension lower than the values considered so far. The former would increase the droplet speed and ensure a stronger impact against the pore, thus likely providing the necessary force to squeeze in, while the latter would diminish the resistance to undergo considerable shape deformations favouring the crossing. In Supplementary Movie 3 we show, for example, the dynamic behavior of a contractile droplet where  $\zeta = -10^{-3}$  and  $\lambda \simeq 0.6$ . Despite raising  $|\zeta|$ , the force is not high enough to guarantee the crossing. Indeed, once near the pore, the droplet

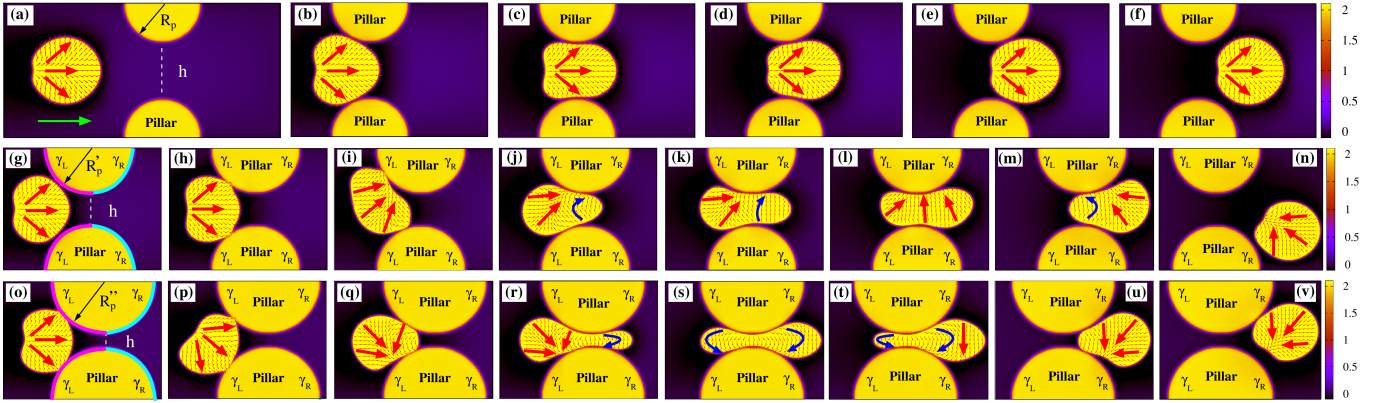


Figure 2. **Transmigration of an active drop across a constriction.** (a)-(f) If the size of the constriction is comparable with that of the droplet ( $\lambda \simeq 0.8$ ,  $h = 72$ ,  $R_p = 49$ ,  $D = 90$ ), the latter moves unidirectionally (the green arrow indicates the direction of motion) undergoing weak shape deformations, such as a slight longitudinal stretching (b) and mild compression (c-d). Out of the constriction, the circular shape is restored (e-f). The splay distortion (highlighted by large red arrows) of the polarization remains essentially unaltered. (g)-(n) If  $\lambda \simeq 0.5$  ( $h = 46$ ,  $R_p' = 62$ ,  $D = 90$ ), the incipient unidirectional motion slows down as the droplet approaches the constriction, where large portions of the fluid interface stick to (g-h) because of adhesion forces, larger at the entry and weaker at the exit (here  $\gamma_L = 3 \times 10^{-2}$ ,  $\gamma_R = 7.5 \times 10^{-3}$ ). Afterwards, the droplet undergoes an intense folding (i) followed by a significant elongation (j-k-l) and decompression (m). Within the constriction, the polarization aligns essentially perpendicularly to the direction of motion, exhibiting a temporary bend deformation (highlighted with blue arrows), initially at the front (j-k) and then shifted towards the back (m). At the exit of the pore, the droplet detaches from the pillars and proceeds along the direction imposed by the splay deformation (n). (o)-(v) If the size of the constriction is very narrow ( $\lambda \simeq 0.2$ ,  $h = 20$ ,  $R_p'' = 75$ ,  $D = 90$ ), the droplet initially adheres to the pillars and then shifts downwards to protrude its leading edge within the pore (o-q). Afterwards, it dramatically stretches along the direction of motion acquiring an initial ampule-like shape (r), subsequently replaced by an intermediate hourglass structure (s). Finally the droplet retracts its rear, pushes its front forward (t) and leaves the pore (u-v), a process facilitated by the lower adhesion forces at the exit (here  $\gamma_L = 2.5 \times 10^{-2}$ ,  $\gamma_R = 10^{-2}$ ). Within the pore, the polar field shows long-lasting bend distortions, either along with splay deformations (r-t) or alone and spread to the whole drop (s).

moves upwards, stretches longitudinally and turns back along the direction imposed by the splay deformation, only temporarily lost during the previous elongation in which  $\mathbf{P}$  becomes approximately uniform. Further increasing  $|\zeta|$  would require the adjustment of other thermodynamic parameters to ensure a correct balance between splay distortions (controlled by  $\kappa$ , see Eq.1) and interfacial tension (controlled by  $a$  and  $k$ ) in order to observe a unidirectional motion.

An alternative route potentially favouring the transmigration is through adhesion forces enhancing the connectivity between the active droplet and the pillars of the constriction. Following microfluidic experiments on transmigration of real cells [44, 46], an adhesive effect could be promoted by functionalizing the pillars with various proteins, such as fibronectin or collagen, while the surrounding area (i.e. the flat walls) would be passivated using chemical repellents. This mechanism could i) minimize the bounce back of the droplet, ii) provide the additional interfacial stress necessary to move the droplet forward as in contact with solid surfaces and iii) facilitate substantial morphological deformations under strong confinement. Such a strategy draws partial inspiration from that of eukaryotic cells crawling on a solid substrate [53], a process in which the anchoring of the

actin cytoskeleton to the surface is controlled by the focal adhesions, clusters of membrane proteins continuously assembled at the cell front and disassembled at the rear during the gliding [52]. Although our active droplet remains distant from a living cell in many aspects, nonetheless it may provide a model for lamellar cell fragments [54, 55] (deprived of the nucleus) or for biomimetic artificial cells with propensity to self propel [12] and capable of crossing micropores with chemically functionalized adhesive surfaces [56].

In Fig.2g-n (and Supplementary Movie 4) we show the dynamics of a motile droplet ( $\zeta = -7 \times 10^{-4}$ ) crossing a constriction where  $\lambda \simeq 0.5$  and in the presence of adhesive forces between the interface of the drop and the surface of the pillars. In our model the strength of the adhesion is controlled by the positive constant  $\gamma$  (see Eq.1), which we set equal between drop and each pillar and patterned following the sketch reported in Fig.2g. We essentially define two values of  $\gamma$ , namely  $\gamma_L$  and  $\gamma_R$  gauging the adhesion of the left and right sides of the pore, with the general constraint that  $\gamma_L > \gamma_R$  and such that  $\gamma = \gamma_L$  for  $0 < y \leq l/2$  and  $\gamma = \gamma_R$  for  $l/2 < y < l$ , being  $y$  the horizontal coordinate and  $l$  the diameter of the pillars. In addition  $\gamma_{\min,L} \leq \gamma_L \leq \gamma_{\max,L}$  and  $\gamma_{\min,R} \leq \gamma_R \leq \gamma_{\max,R}$ , where  $\gamma_{\min,L}$ ,  $\gamma_{\max,L}$ ,  $\gamma_{\min,R}$ ,

$\gamma_{\max,R}$  represent critical values depending on the details of the simulations (such as speed of the drop, elasticity and size of the pore) beyond which the crossing is generally inhibited. In Fig.2g-n we have  $\gamma_L = 3 \times 10^{-2}$  (with  $\gamma_{\min,L} \simeq 2 \times 10^{-2}$ ,  $\gamma_{\max,L} \simeq 5 \times 10^{-2}$ ) and  $\gamma_R = 7.5 \times 10^{-3}$  (with  $\gamma_{\min,R} \simeq 5 \times 10^{-3}$ ,  $\gamma_{\max,R} \simeq 2 \times 10^{-2}$ , see also Supplementary Note 3 for further results). Such a design essentially allows for higher adhesion forces at the entrance of the constriction and weaker ones at the exit, thus potentially enabling the transmigration. In Supplementary Note 4 we show that the physics remains qualitatively similar if a smoother variation of  $\gamma$  between entry and exit of the constriction is considered.

Once the droplet approaches the pore, small portions of its interface hit opposite pillars and adhere to their surfaces (Fig.2g,h), thus causing a progressive slowdown and a light deviation from the rectilinear trajectory (see Fig.3b and Fig.3k). Afterwards, the drop moves upward due to an internal fluid vortex (see the section on the fluid structure for a detailed description), an effect not sufficient to determine its detachment from the pillars but crucial to drive morphological changes necessary to squeeze into the gap (Fig.2i,j,k,l). Indeed, the droplet initially stretches pushing its front within the constriction and then elongates longitudinally dragging the rear, thus causing an increase of its perimeter (see the next paragraph about the energetic balance). On the contrary, the droplet area (i.e.  $\phi_1$ ) is conserved, since its evolution is governed by a model B-like dynamics (see the section Methods). During such process, the speed undergoes a sharp increase (Fig.3l-m) followed by a steep reduction (Fig.3n), yielding a temporary freezing of the droplet shape into a peanutlike structure, where opposite sides of its interface remain firmly anchored at the surface of the pillars. However adhesion forces at its front are weaker than those at the rear ( $\gamma_R < \gamma_L$ ), an effect that can facilitate crossing and detachment of the droplet if a sufficient propulsion force operates. This is precisely the dynamics observed in the final stage of the process, where the droplet slowly decompresses while leaving the pore (Fig.2m,n) and its center of mass speed raises once again (Fig.3o). Finally note that, along with splay distortions (generally the dominant contribution far from the constriction), the confined environment of the pore triggers the formation of regions where the polar field exhibits temporary bend deformations (Fig.3m,n, blue arrows), an arrangement generally emerging as an elastic instability in extensible material [1], here easier to accommodate in such a highly stretched geometry. Interestingly, even though the interface anchoring remains largely perpendicular, a tangential orientation arises where droplet elongation increases, an effect mainly observed at the entry and the exit of the pore.

The results discussed so far suggest that higher values of adhesion force at the entrance and lower ones at the exit of the gap can favour the transmigration. If, alter-

natively, the adhesion between the droplet interface and the surface of the pillars is uniform everywhere the crossing can be inhibited, as shown in Supplementary Movie 5 where  $\lambda \simeq 0.5$ ,  $\zeta = -8 \times 10^{-4}$  and  $\gamma_L = \gamma_R = 0.03$ . Once again, a series of shape modifications, driven by a combination of contractility, elastic deformations of polarization and fluid interface plus adhesion forces, allows the active droplet to squeeze into the pore. However, higher values of  $\gamma_R$  at the exit of the constriction prevent the migration, permanently sequestering the droplet in the middle of the gap. Note that this outcome is in agreement with the constraint on  $\gamma_R$ , since here  $\gamma_R > \gamma_{\max,R}$ .

### Motile droplet across a narrow interstice.

Further diminishing  $\lambda$  leads to a higher complex behavior where adhesion forces, once more, are found to play a decisive role. In Fig.2o-v (and Supplementary Movie 6) we show the time evolution of an active droplet crossing a constriction with  $\lambda \simeq 0.2$ ,  $\zeta = -7 \times 10^{-4}$ ,  $\gamma_L = 2.5 \times 10^{-2}$  and  $\gamma_R = 10^{-2}$ . Here,  $\gamma_{\min,L} \simeq 2 \times 10^{-2}$  and  $\gamma_{\max,L} \simeq 4 \times 10^{-2}$ , while  $\gamma_{\min,R} \simeq 5 \times 10^{-3}$  and  $\gamma_{\max,R} \simeq 1.5 \times 10^{-2}$ . Note that the narrowing of the pore shrinks the range of values of  $\gamma$  enabling the crossing. The initial stage of the process follows a dynamics akin to that observed for a mild constriction ( $\lambda \simeq 0.5$ ). Indeed, once portions of interfaces adhere to the surface of the pillars (Fig.2o), the droplet slows down (Fig.3p) and shifts downwards (Fig.2p) essentially preserving the arrangement of the internal polarization. Afterwards, the speed increases (Fig.3q,r,s) and the front squeezes into the interstice (Fig.2q) but, unlike the pore of larger size, here the droplet undergoes a dramatic stretching. Indeed, it provisionally acquires an ampule-like shape (Fig.2r) subsequently replaced by a hourglass structure made of two rounded blobs of approximately similar size located near the entrance and the exit of the pore (Fig.2s). Then, its rear retracts within the orifice while the front protrudes out of the pore and broadens, leading to a long-lasting ampule shape moving at very low speed. At this stage the velocity sharply diminishes (Fig.3t) basically because of lack of sufficient propulsion fostered by large splay distortions. Note in particular that, during the course of the crossing, a relevant bend deformation emerges, initially solely at the front (Fig.2r), then spread to the whole droplet (Fig.2s), and finally confined at the back (Fig.2t) together with splay distortions. At the fluid interface, especially nearby the two bulges, the polar field displays a preferential tangential orientation, an effect sharper than that observed in wider constrictions due to the narrowing of the gap. At the exit, the lower adhesion forces between the surface of pillars and the interface allow the droplet to gain a high enough speed (Fig.3u) and leave the constriction (Fig.2u,v), while the shape progressively turns to circular and the splay distortion becomes dom-

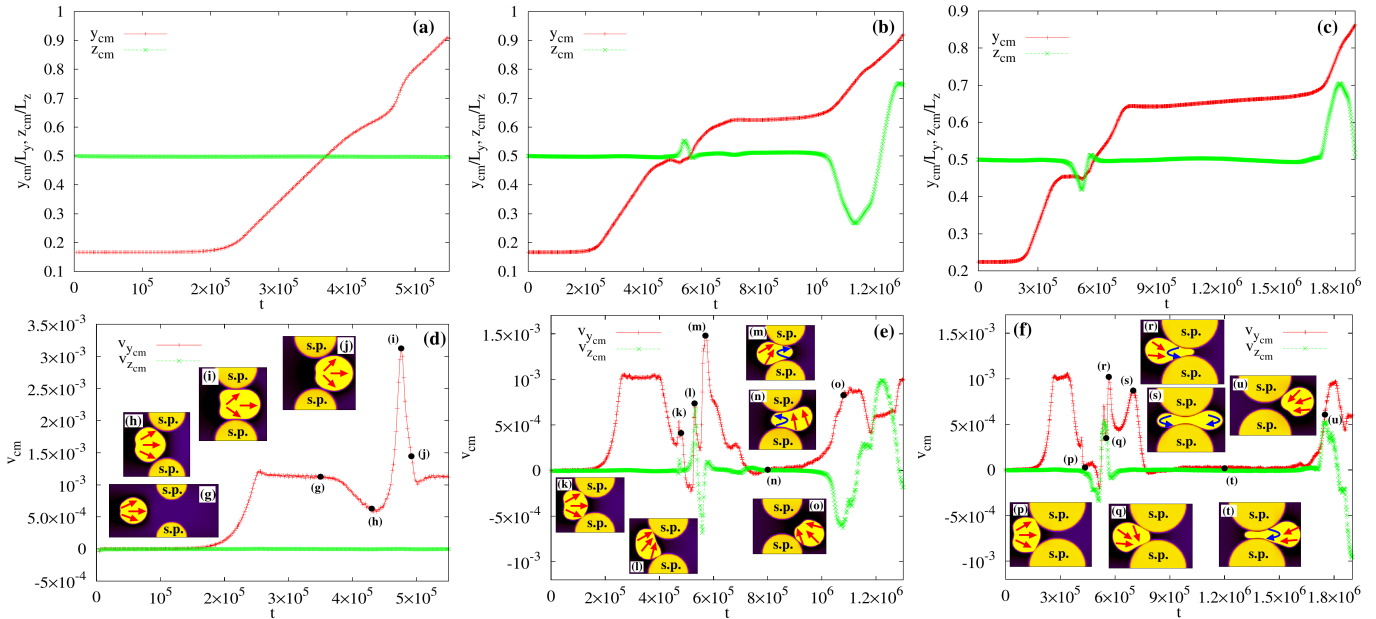


Figure 3. **Center of mass position and speed of the active drop for different pore sizes.** Top row: Time evolution of the  $y$  (red, pluses) and  $z$  (green, crosses) components of the center of mass of the active droplet for  $\lambda \simeq 0.8$  (a),  $\lambda \simeq 0.5$  (b) and  $\lambda \simeq 0.2$  (c). Bottom row: Time evolution of  $y$  (red, pluses) and  $z$  (green, crosses) components of the speed of the center of mass for  $\lambda \simeq 0.8$  (d),  $\lambda \simeq 0.5$  (e) and  $\lambda \simeq 0.2$  (f). Black dots indicate the position of the insets representing instantaneous configurations observed during the crossing. Red arrows show the direction of the splay deformations while blue ones that of the bending. Also, "s.p." stands for solid pillars. If  $\lambda \simeq 0.8$ , the droplet proceeds almost unaltered along its unidirectional trajectory, progressively decreasing the speed at the entrance of the pore (g,h) and rapidly augmenting it in the middle (i,j), where shape deformations are larger. If  $\lambda \simeq 0.5$ , the speed diminishes at the entrance of the constriction (k) and then rapidly augments (l,m), as the droplet front squeezes into the pore. Afterwards, the speed undergoes a second sharp decrease (n), considerably slowing down the droplet but only temporary arresting its motion. It gradually starts over (o) due to internal fluid flows caused by the contractile material. Note that, alongside the usual splay deformation, temporary bend distortions emerge (blue arrows), initially located at the front and progressively shifted backwards. If  $\lambda \simeq 0.2$ , once again the decrease of the droplet speed at the entrance of the pore (p) is followed by its quick rise once the tip of the drop squeezes in (q,r) and moves forward (s). Here, bend deformations persist longer than before and spread over the entire drop in the middle of the pore. Then, the speed undergoes a second quick reduction freezing the drop into an ampule-like shape (t) for a long period of time, after which the transmigration is completed (u).

inant. It is worth highlighting that the speed reduction in the gap and the raise at the exit are generic features observed regardless of the size of the constriction, a result in agreement with experiments of transmigration of 3d cells [44].

### Fluid structure interaction

A deeper understanding of the dynamics of the transmigration can be gained by the evaluation of the fluid-structure interaction, especially for mild and narrow constrictions where morphological deformations are considerably higher than those observed in larger pores. In Fig.4 and Fig.5 we show the fluid velocity  $\mathbf{v}$  (top row) and its magnitude  $|\mathbf{v}|$  (bottom row) for  $\lambda \simeq 0.5$  and  $\lambda \simeq 0.2$ , respectively, within the droplet and in the surrounding environment. Clearly, the structure of the fluid flow in these cases considerably departs from that of a droplet swimming in an unconstrained system (see Fig.1g), where

a couple of counter-rotating vortices sustains the motion. If, for example,  $\lambda \simeq 0.5$ , only a single counterclockwise vortex survives as the drop approaches the pore (Fig.4a). During the transmigration, a unidirectional flow emerges at the front (Fig.4b,c) pushing the vortex backwards, until they merge producing a homogeneous oscillating pattern (Fig.4d). Interestingly, a similar structure has been also observed in experiments of tumor cells in which the displacement within a micro-environment is driven by an osmotic pressure difference across the membrane, causing a net flow from the leading edge of the cell to the rear [57]. Note that the magnitude of the velocity is particularly high at the interfaces in contact with pillars (Fig.4f,g,h,i), an effect indicating that the adhesion is crucial to provide the excess of kinetic energy necessary to push the droplet within the constriction and enable its transmigration. Once at the exit of the pore, the double vortex structure is restored (Fig.4e) and  $|\mathbf{v}|$  decreases about one order of magnitude within the drop (Fig.4j).

If  $\lambda \simeq 0.2$ , once again the typical double vortex ob-

served at the entrance of the gap shifts towards the rear as the drop sneaks into the pore (Fig.5a,b). However, since the high confinement prevents the formation of fluid structures larger than the gap size, the vortices turn into a rectilinear flow exhibiting a four-fold symmetric structure (Fig.5c). Such flow progressively weakens as the drop moves forward (a condition favoured by the lower adhesion forces at the exit of the pore), and is gradually replaced by the double vortex, fully reestablished at the exit (Fig.5d,e). As in the medium size constriction, the highest values of the velocity field are found along the interfaces in contact with the pillars, where adhesion forces operate (Fig.5f,g,h,i,j). Note finally that the velocity field, besides critically affecting the shape of the active droplet, profoundly depends on the structure of the underlying polar field, essentially regardless of the size of the constriction. In fact, while the double vortex pattern emerges in the presence of splay distortions, a rectilinear (often unidirectional) flow is produced when bend deformations are dominant.

The effects due to shape changes, modifications of orientation of the active material as well as adhesion forces can be quantitatively gauged by computing the associated free energy contributions reported in Eq.1. This is discussed in the next section.

### Energetic balance

In Fig.6 we show the time evolution of  $F_{\text{el}}^{\text{bf}} = \int k/2(\nabla\phi_1)^2$  assessing the interfacial energy of the droplet,  $F_{\text{el}}^{\text{lc}} = \int \kappa/2(\nabla\mathbf{P})^2$  accounting for the deformations of the polarization and  $F_{\text{ad}} = \int \sum_{i,j,i < j} \gamma \nabla\phi_i \nabla\phi_j$  quantifying the adhesion contribution. We start from  $\lambda \simeq 0.5$  (left panel). As discussed in Fig.1, once the activity  $\zeta$  is turned on, the drop initially elongates axially attaining a motionless elliptical shape and then acquires motion due to a spontaneous flow causing a symmetry breaking of the polar field. In the former regime both  $F_{\text{el}}^{\text{bf}}$  (Fig.6m) and  $F_{\text{el}}^{\text{lc}}$  (Fig.6o) increase and stabilize (for  $t \leq 2 \times 10^5$ ), whereas in the latter (i.e. as the droplet starts to move)  $F_{\text{el}}^{\text{bf}}$  lowers, since the drop turns to an approximately circular shape, and  $F_{\text{el}}^{\text{lc}}$  augments due to the presence of splay deformations. Then they both attain a value kept constant until the drop approaches the pore (at  $t \simeq 4.5 \times 10^5$ ). Note that in these regimes  $F_{\text{ad}}$  (Fig.6q) remains essentially zero since drops and pillars are sufficiently far away from each other.

At the entry of the constriction, the droplet deforms (Fig.6a,b,c) and elongates to squeeze in (Fig.6d), thus causing a further increase of  $F_{\text{el}}^{\text{bf}}$  (capturing the growth of interfacial area), which attains its maximum value approximately in the middle of the pore. On the contrary,  $F_{\text{el}}^{\text{lc}}$  initially decreases since the splay distortion slightly weakens, and then it rapidly augments, especially when bend deformations appear at the front. Once at the exit

of the pore, the droplet decompresses and the liquid crystal deformations turn milder (Fig.6e,f), thus both free energy contributions gradually reduce to values comparable with those hold before the crossing. During such process  $F_{\text{ad}}$  turns negative when the drop interface starts to adhere to the pillars, attaining its higher (absolute) values at the entry (Fig.6a) and within the pore (Fig.6c,d), basically because larger portions of interfaces are in close contact with the pillars.

If the size of the constriction decreases ( $\lambda \simeq 0.2$ , Fig.6n,q,p),  $F_{\text{el}}^{\text{bf}}$ ,  $F_{\text{el}}^{\text{lc}}$  and  $F_{\text{ad}}$  show a time evolution akin to that discussed previously, albeit larger values are observed when the drop crosses the pore. Indeed,  $F_{\text{el}}^{\text{bf}}$  and  $F_{\text{el}}^{\text{lc}}$  rise, once again, at the entrance of the gap (Fig.6g), slightly decrease later since elastic deformations gets globally milder (Fig.6h), and then considerably augmented up to a maximum (almost doubling the values observed for a drop migrating freely in the microchannel), when the drop front squeezes in (Fig.6i,j) and attains a hourglass shape. Afterwards,  $F_{\text{el}}^{\text{bf}}$  and  $F_{\text{el}}^{\text{lc}}$  continuously diminish (Fig.6k,l) until the drop has left the pore. As in the previous case,  $F_{\text{ad}}$  turns negative once the interface adheres to the pillars, and its larger values are obtained basically when the drop displays the ampule and the hourglass shape.

### Dimensionless numbers

Further insights on the transmigration can be gained by analyzing the physics in terms of a suitable set of dimensionless quantities. Common numbers used in droplet microfluidics are the Reynolds and capillary ones, defined as  $\text{Re} = \rho v D / \eta$  and  $\text{Ca} = v \eta / \sigma$ , where  $\rho$  is the fluid density,  $v$  is the droplet speed,  $\eta$  is the fluid viscosity and  $\sigma$  is the surface tension (see also Supplementary Notes 1 and 2 for further details on specific values). The former represents the ratio of inertial forces to viscous ones and, in our simulations, it is generally equal or below 0.1, thus well within the laminar regime. The latter measures the effect of viscous force (favoring shape deformations) versus surface tension ones (which oppose shape changes), and is approximately equal to 0.1 (or lower). This value ensures that droplet breakup is an unlikely event.

In addition, we consider the following three quantities: the Ericksen number  $\text{Er} = \zeta R^2 / \kappa$ , the adhesion number  $\text{A} = \gamma_{\text{L}} / \gamma_{\text{R}}$  and the inertia over adhesion number  $\text{I}_{\text{A,L,R}} = \rho v^2 R^2 / \gamma_{\text{L,R}}$ . The former controls the dynamics at the onset of the spontaneous motion far from the constriction. More specifically, if  $\text{Er} > 1$  the active forces are sufficiently large to overcome the elasticity of the liquid crystal (mediated elastic constant  $\kappa$ ) and destabilize the droplet, finally inducing spontaneous motion. In our simulations,  $\text{Er}$  is generally larger than 5, thus high enough to trigger self-locomotion. The adhe-



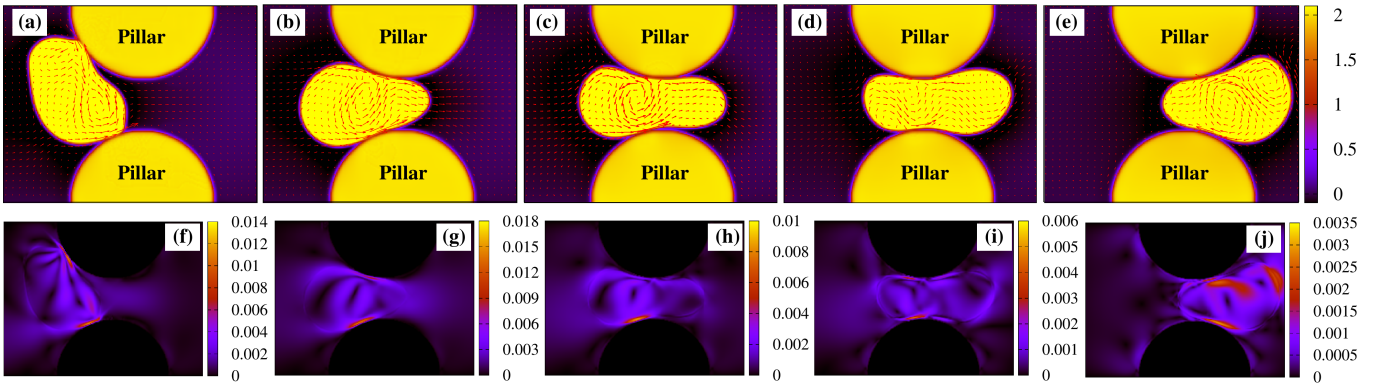


Figure 4. **Velocity field in a medium size constriction.** The top row (a-e) shows the structure of the velocity field  $\mathbf{v}$  within and in the surrounding of an active droplet crossing a constriction where  $\lambda \simeq 0.5$ , while the bottom one shows its magnitude  $|\mathbf{v}|$ . The double vortex pattern observed in the unconstrained motile droplet (see Fig.1g) turns into a single one rotating counterclockwise (a), with magnitude larger near the pillars (f). Once the droplet enters the pore, such vortex shifts towards the center of the drop, while a net unidirectional flow emerges at the front (b,c) and becomes dominant near the exit (d), where it acquires an oscillating structure. During the crossing the magnitude  $|\mathbf{v}|$  remains higher near the pillars (g,h,i), whereas it considerably decreases at the exit (j), once the double vortex structure is restored (e).

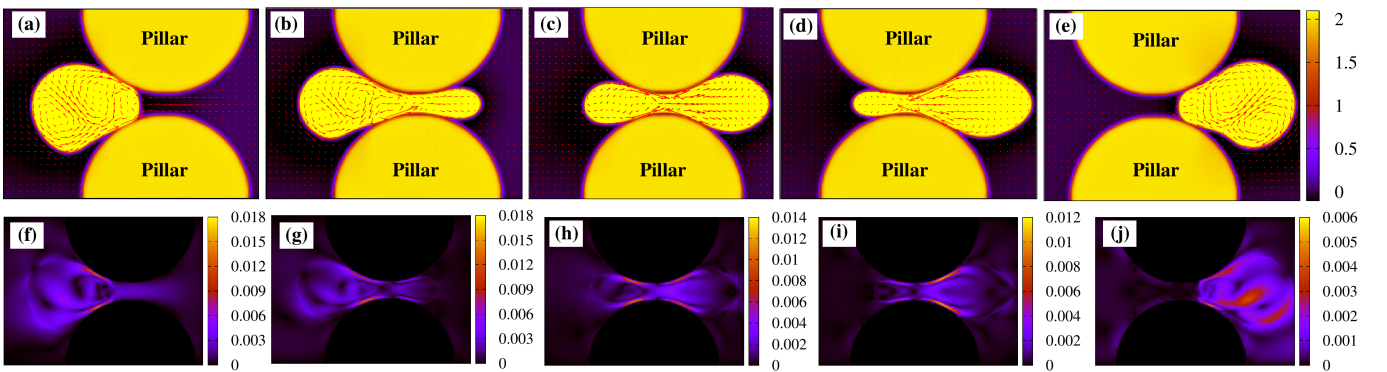


Figure 5. **Velocity field in a narrow constriction.** The top row (a-e) shows the velocity field  $\mathbf{v}$  during the transmigration with  $\lambda \simeq 0.2$ , while the bottom one shows its magnitude  $|\mathbf{v}|$ . Here, the double vortex pattern (a) moves progressively backwards (b) until it is temporarily replaced, in the middle of the pore, by a squeezed four-fold symmetric structure, in which a unidirectional flow pushing the drop forward still prevails (c). Once the droplet leaves the pore, the double vortex gradually recovers, initially confined at the front (d) and afterwards spread within the bulk (e). Once again, the magnitude of  $\mathbf{v}$  remains high especially near the surfaces of the pillars (f,g,h,i), while substantially diminishing as the droplet leaves the constriction (j).

sion number  $A$  represents the balance between adhesion forces at the entry and the exit of the pore and, for a successful transmigration, it must be strictly larger than 1 (since  $\gamma_L > \gamma_R$ ). For  $\lambda \simeq 0.5$ , we get  $2 \lesssim A \lesssim 10$ , while for  $\lambda \simeq 0.2$  we have  $2 \lesssim A \lesssim 3$ , a narrower range of values due to the reduction of the size of the pore. Finally, the number  $I_{A,L,R}$  gauges the importance of inertial forces over adhesive ones. For  $\lambda \simeq 0.5$  and  $\gamma_R = 5 \times 10^{-3}$  (a value for which the crossing occurs), one has  $I_{A,R} \simeq 0.25$  and  $0.025 \lesssim I_{A,L} \lesssim 0.06$  (assuming a droplet speed  $v \simeq 5 \times 10^{-4}$ ). This means that, at the entry, inertial forces are much weaker than adhesive ones, a necessary condition to keep the droplet attached to the pillars and enable the crossing. The opposite is true at the exit, where lower adhesion forces allow a droplet with sufficiently high speed to escape from the pore. For

$\lambda \simeq 0.2$ , similar considerations hold. Here, if  $\gamma_R = 10^{-2}$ , one has  $I_{A,R} \simeq 0.1$  and  $0.04 \lesssim I_{A,L} \lesssim 0.06$ .

### Transmigration order parameter

Inspired by the Lubensky-Nelson model of polymer translocation through nanopores [58], before concluding we provide a characterization of the droplet transmigration in terms of a single order parameter-like quantity  $\chi(t) = A_C(t)/A_T(t)$ , defined as the ratio between the area fraction  $A_C(t) = \int_{l/2}^l \phi_1(\mathbf{r}, t) d\mathbf{r}$  of droplet that has transmigrated the centerline of a pore of length  $l$  and the total area  $A_T(t) = \int_0^l \phi_1(\mathbf{r}, t) d\mathbf{r}$  of the droplet within the pore. It varies between 0 (the droplet has not passed the midline) and 1 (the whole droplet has overcome the

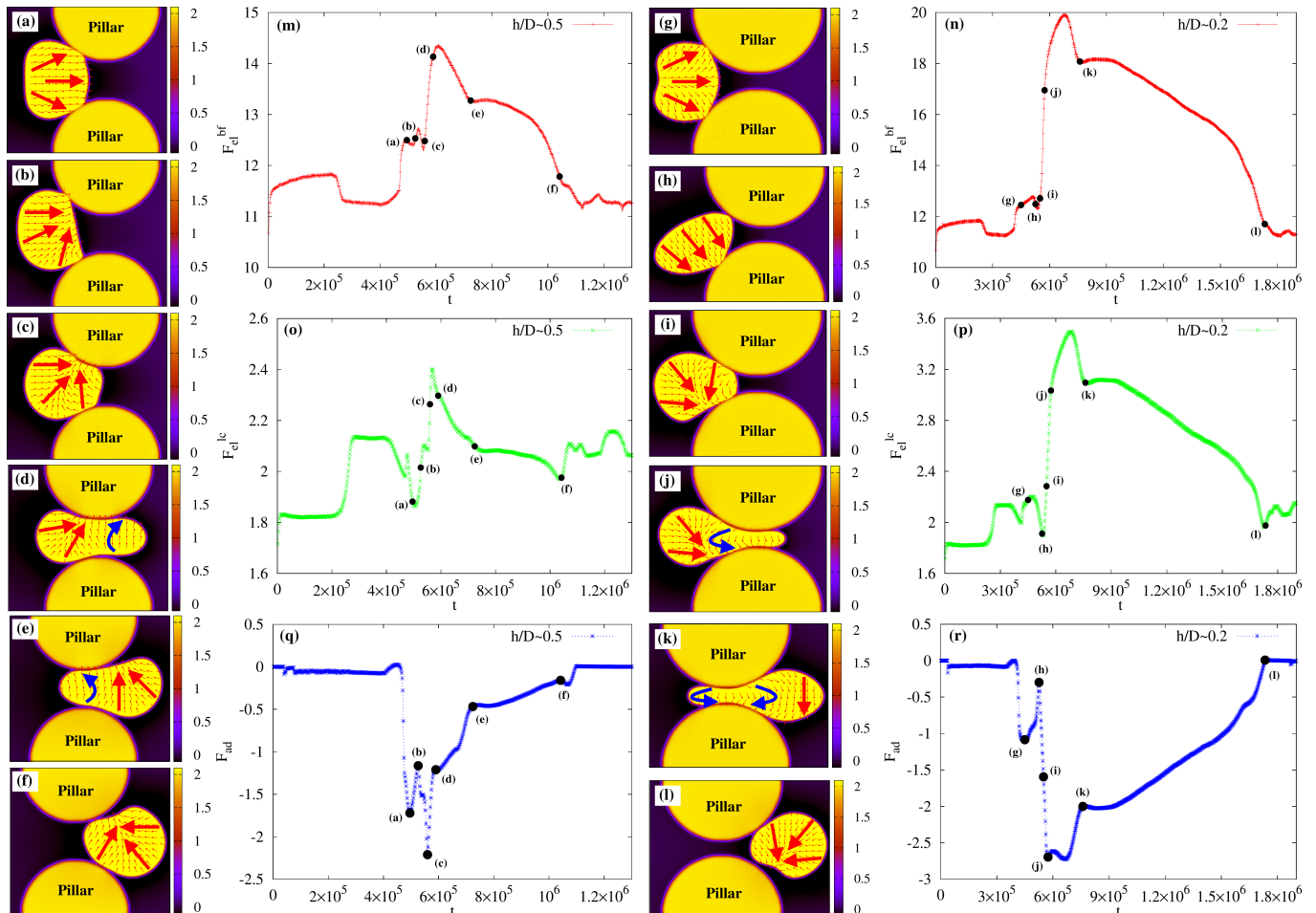


Figure 6. **Free energy.** The plots show the time evolution of the elastic free energy  $F_{el}^{bf} = \int k/2(\nabla\phi_1)^2$  of the binary fluid (top line, red pluses), the elastic free energy  $F_{el}^{lc} = \int \kappa/2(\nabla\mathbf{P})^2$  of the polar liquid crystal (green, crosses) and the adhesion contribution  $F_{ad} = \int \sum_{i,j,i < j} \gamma \nabla\phi_i \nabla\phi_j$  (blue, asterisks). Black dots indicate the instantaneous configurations of the active droplet during the transmigration for  $\lambda \simeq 0.5$  (left side) and  $\lambda \simeq 0.2$  (right side). If  $\lambda \simeq 0.5$ , the droplet adheres to pillars and deforms (a,b,c), thus causing an increase of  $F_{el}^{bf}$  (m) with respect to the values attained during the unconstrained motile state (for  $t \leq 4.5 \times 10^5$ ). On the contrary,  $F_{el}^{lc}$  (o) displays an initial descent due to a slight drop of splay followed by a quick growth, since bend distortions start to appear. Once the drop snakes into the pore (d), such contributions further augment since a higher stretching entails larger bend distortions, whereas near the exit they diminish (e,f), as bend essentially disappears and the droplet reacquires a crescent-like shape with mild deformations.  $F_{ad}$  (q) is zero when the drop is far from the pore, while it turns negative as its interface comes in contact with the pillars. In particular,  $F_{ad}$  attains lower values during the squeezing and the subsequent crossing (a,b,c,d), whereas it gets progressively smaller once the drop approaches the exit and leaves the pore (e,f). If  $\lambda \simeq 0.2$ ,  $F_{el}^{bf}$  (n), out of the pore (g,h,i,l)  $F_{el}^{lc}$  (p) and  $F_{ad}$  (r) exhibit a behavior akin to that observed for a larger constriction while, during the crossing (j,k), their (absolute) values are generally higher, ultimately because shape deformations and liquid crystal distortions (including splay and bend contributions) are considerably heavier and persist over a longer period of time.

midline). In Fig.7 we show the time evolution of  $\chi(t)$  for different values of  $\lambda$ , in simulations where  $\zeta \simeq -7 \times 10^{-4}$ ,  $2.5 \times 10^{-2} \leq \gamma_L \leq 3 \times 10^{-2}$  and  $7.5 \times 10^{-3} \leq \gamma_R \leq 10^{-2}$ . If the constriction is wide enough ( $\lambda \simeq 0.8$ ),  $\chi(t)$  exhibits a ballisticlike behavior rapidly growing towards 1 essentially with a single slope. On the contrary, if the size of the constriction diminishes, the crossing occurs over longer periods of time, which augments for decreasing values of  $\lambda$ . In these systems  $\chi(t)$  displays basically three regimes, i) a fast-growing approximately linear one

at the entry of the pore, ii) a transient stationary one roughly in the middle of the constriction and iii) a final slower monotonic regrowth at the exit. While in the first regime the transmigration proceeds rather quickly (more than half of the droplet has overcome the midline,  $\chi \geq 0.5$ ) basically because of a combination of droplet propulsion, splay deformations of the liquid crystal and adhesion with the pore, later on the process dramatically slows down and the droplet attains an almost non-motile state (see also Fig.2). Here, the slope of  $\chi(t)$

turns slightly negative (for  $\lambda \simeq 0.5$  and  $\lambda \simeq 0.2$ ) due to a temporary retraction of the droplet and then exhibits short-lived plateaus, lasting longer for smaller  $\lambda$ . In the last regime, the transmigration restarts and, as expected, occurs faster for larger  $\lambda$  although at a speed much smaller than the one at the entry (in agreement with the results of Fig.4 and Fig.5).

Finally, computing  $\chi(t)$  may provide insights about the time employed by an active droplet to cross a constriction. Indeed, assuming that one simulation timestep corresponds to  $T = 10\text{ms}$  in real units (further details about the mapping to real values are in Supplementary Note 2), the crossing time  $T_c$  ranges approximately between 1.5 hours for  $\lambda \simeq 0.5$  and 3 hours for  $\lambda \simeq 0.2$ , numbers in qualitative agreement with the ones found, for example, in fibroblasts crossing narrow interstices [44].

These results suggest that, despite the complex physics involved, a single collective variable, measuring the progress of the crossing, is capable of conveying remarkable insights about the process, such as rapidity of the transmigration through different regions of the pore, retraction of the droplet and stationary regimes occurring especially within narrow interstices.

## DISCUSSION

In summary, we have numerically studied the physics of an active gel droplet migrating through a constriction, mimicking conditions potentially reproducible in microfluidic experiments. Key ingredients of the model are the contractility of the polar liquid crystal confined within the drop and the adhesiveness between the fluid interface and the solid surfaces modelling the pore. In addition, hydrodynamic interactions are properly incorporated throughout the model.

We have shown that, if the height  $h$  of the constriction is comparable with the diameter  $D$  of the droplet, a careful control of droplet speed and elasticity (i.e. interfacial tension and elastic deformation of the active fluid) are sufficient to guarantee a smooth crossing. On the contrary, if  $h$  becomes considerably smaller than  $D$  (i.e.  $\lambda \lesssim 0.5$ ), adhesion forces between the interface of the drop and the pillars of the pore are decisive to enable the crossing. Our results suggest that a stronger adhesion at the entry and a lower one at the exit of the constriction favours the transmigration in conditions that would have been inhibited otherwise. The process entails considerable morphological changes, ranging from crescent to ampule and hourglass-like geometries (structures akin to the ones observed, in similar conditions, in tumor breast cells [59, 60]), alongside substantial deformations of the contractile material, including the concurrent presence of splay and bend distortions, the latter generally higher for narrower orifices. The formation of such striking variety of shapes as well as the ordering properties of the con-

tractile material are tightly linked to the fluid structure, which is found to exhibit two dominating patterns: i) long-lasting vortices out of the constriction, only temporarily surviving within the pore, and ii) short-lived rectilinear flows in the orifice. Hence, the combined effect of confinement and adhesion is to rectify the flow within the constriction, a condition that ultimately enables the transmigration. We highlight that the general picture emerging from these results qualitatively holds if a frictional force is included (see Supplementary Note 5). This extra term would mimic, in a phenomenological way, the momentum sink due to the presence of walls placed at an infinitesimal small distance, as in a thin film.

On an experimental side, these results can be reproduced by using microfluidic techniques already adopted to study the transmigration of biological cells [44, 61]. Our system could be mapped onto a micro-channel of length 0.5-1mm equipped with PDMS solid pillars, whose surfaces are placed at distance ranging from  $10\mu\text{m}$  to  $70\mu\text{m}$  and functionalized with proteins (such as collagen or fibronectin) favouring droplet adhesion. Two different concentrations of such proteins could model the change of adhesion strength at the entry and exit of the constriction. A self-propelled micrometer droplet of  $D \simeq 90\mu\text{m}$  and moving at speed from  $1\mu\text{m/s}$  up to  $10\mu\text{m/s}$  can be self assembled by encapsulating an active polar gel (with effective viscosity  $\eta_{eff} \simeq 1.5\text{kPa}\cdot\text{s}$  and elastic constant  $\kappa \simeq 4\text{nN}$ ) within a water-in-oil emulsions, following the formulation of Ref.[12]. Further details can be found in Methods and Supplementary Note 3.

Besides providing a deeper understanding of the physics of active fluid droplets migrating in constrained environments, our results may prove useful for the realization of bio-inspired artificial swimmers capable of transporting cargoes to specific locations, a process of interest in drug delivery in which one needs to efficiently load pharmaceutical molecules without compromising the structural integrity of the carrier, especially when moving through microscale constrictions. In addition, since some aspects of this active droplet resemble those of laminar cell fragments [54, 55], our results could provide insights for ameliorating the design of microfluidic cell sorting devices, which make use of surfaces patterned with specific adhesive properties to detect and isolate cells [56]. Yet, our model remains distant from a living cell in many aspects, such as the lack of the nucleus and of the complex underlying biochemical network governing, for example, the mechanics of the focal adhesions [53]. Such drawback could be partially overcome by considering a slightly more realistic description of a cell, modeled as a double emulsion [62] in which the inner droplet provides a highly simplified representation of a nucleus and the contractile material is confined within the layer, mimicking the tiny cortex of eukaryotic cells containing the actin cytoskeleton. On a biological side this could be of interest, for example, for studying the

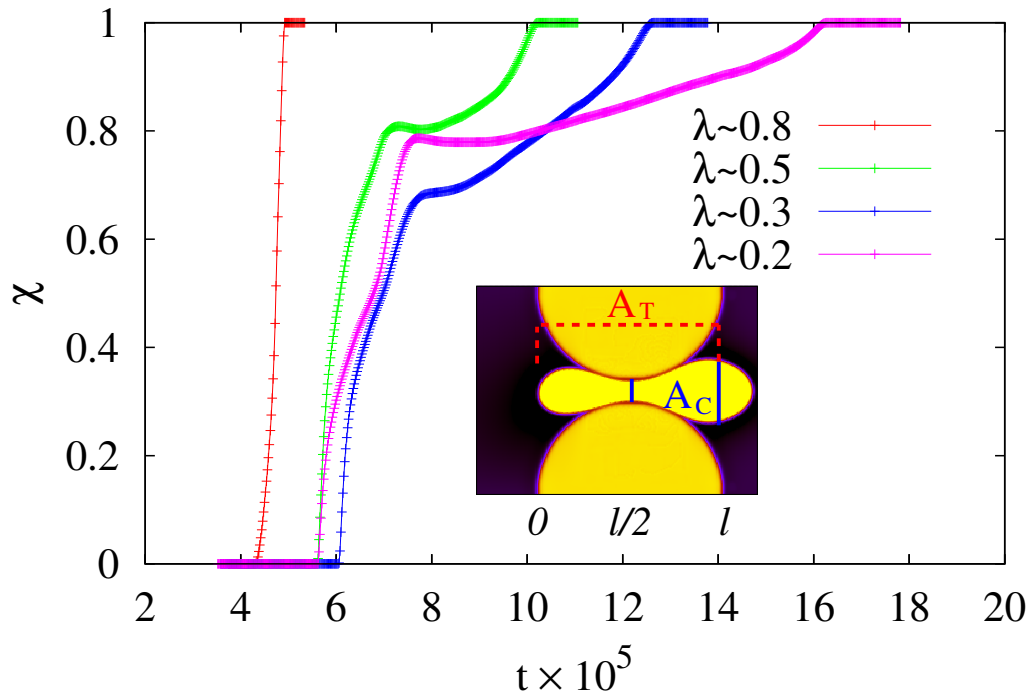


Figure 7. **Transmigration order parameter.** We plot the time evolution of  $\chi(t) = A_C(t)/A_T(t)$ , where  $A_C$  represents the area fraction of droplet between the centerline (located at  $l/2$ ) and the exit of the pore (placed at  $l$ ), and  $A_T$  is the total area of the droplet within the pore. If  $\lambda \simeq 0.8$ ,  $\chi(t)$  grows rapidly towards 1 following an approximately linear behavior. For decreasing values of  $\chi$  one can distinguish three regimes: a fast-growing approximately linear one at the entry of the pore, a short stationary one (lasting longer for narrower interstices) with a temporary negative slope in the middle, and a final slow-growing one at the exit. The inner snapshot shows an instantaneous configuration of the transmigration with  $\lambda \simeq 0.2$ .

effect of physical confinement on tumor cells (such as metastatic breast cancer), where the transmigration has been found to occur even when actin polymerization or myosin contractility are inhibited [57]. In spite of these limitations, our results may support the view that some aspects of droplet migration through constrained environments would strongly rely upon mesoscopic physical ingredients, such as speed, elasticity and adhesion forces rather than on the microscopic details of the physics involved. We finally mention that an alternative class of model systems, potentially useful for designing artificial swimmers, is that of active vesicles, which are built by encapsulating self-propelled particles within a soft membrane [63–65]. Such objects have been found to reproduce some features of motile cells, including membrane fluctuations and highly branched sub-micrometer protrusions, phenomena occurring at lengthscales usually inaccessible by exclusive mean-field like approaches but often crucial in driving pathological processes (such as cancer metastasis) within highly confined environments.

## METHODS

### Basic idea of the model

Here we shortly outline the hydrodynamic model used in this work. We consider a self-propelled fluid droplet containing an active polar liquid crystal (or an active gel) immersed in a passive fluid. The active gel concentration is described in terms of a scalar field  $\phi_1(\mathbf{r}, t)$ , positive within the drop and zero outside. The environment surrounding the droplet is a further passive fluid modeling a wet solvent. Such a mixture is embedded within a microfluidic channel made of two flat parallel walls plus two semi-circular symmetric pillars forming a narrow constriction (see Fig.1). Unlike the flat walls (implemented using no-slip conditions [66], see Supplementary Note 1), the solid structure of the pillars is modeled using two auxiliary *static* phase fields  $\phi_2(\mathbf{r})$  and  $\phi_3(\mathbf{r})$ , positive within each pillar and zero outside. Although this approach provides an approximate description of a constriction, it allows for a relatively easy computational implementation of mesoscale physical effects occurring between drops and pillars (such as the repulsion and the adhesion of the fluid interface with a wall) by minimally modifying a pore-free model already used in previous

studies [20, 25]. As mentioned above, our active drop also hosts a contractile gel whose experimental realization is, for example, an acto-myosin solution. Its mesoscale order is captured by a polar liquid crystal field  $\mathbf{P}(\mathbf{r}, t)$  representing a coarse grained average of all orientations of the internal constituents (e.g. an actin filament). This vector field is positive within the droplet and zero anywhere else. Finally a further vector field  $\mathbf{v}(\mathbf{r}, t)$  describes the global fluid velocity of both drop and solvent.

### Free energy

The equilibrium properties of a purely passive system are encoded in a coarse-grained free energy density [62]

$$\begin{aligned}
 f = & \frac{a}{4\phi_{cr}^4} \sum_i^N \phi_i^2 (\phi_i - \phi_0)^2 + \frac{k}{2} \sum_i^N (\nabla \phi_i)^2 \\
 & - \frac{\alpha}{2} \sum_i^N \frac{(\phi_i - \phi_{cr})}{\phi_{cr}} |\mathbf{P}_i|^2 + \frac{\alpha}{4} \sum_i^N |\mathbf{P}_i|^4 + \frac{\kappa}{2} \sum_i^N (\nabla \mathbf{P}_i)^2 \\
 & + \sum_{i,j,i < j} \epsilon_{ij} \phi_i \phi_j + \sum_{i,j,i < j} \gamma_{ij} \nabla \phi_i \nabla \phi_j, \quad (1)
 \end{aligned}$$

where  $i = 1, 2, 3$  and  $N$  is the total number of phases, i.e. the active drop and the two pillars. Note that, since the polarization is confined within the droplet, the sole nonzero term is  $\mathbf{P}_1$ , whereas  $\mathbf{P}_2 = 0$  and  $\mathbf{P}_3 = 0$ . Hereafter (and in the text as well) we set  $\mathbf{P}_1 = \mathbf{P}$ .

Equation 1 combines three principal contributions, the first two terms stemming from a typical binary fluid formalism, the following three terms borrowed from liquid crystal theory and the remaining part gauging the interaction between the active drop and the pore. In particular the first term of Equation 1 multiplied by the positive constant  $a$  ensures the existence of two coexisting minima,  $\phi_i = \phi_{eq}$  inside the  $i$ -th phase and  $\phi_i = 0$  outside, while the second one determines the interfacial tension whose strength depends on the positive constant  $k$  and reads  $\sigma = \sqrt{8ak}/9$ . The following contributions, comprising the terms multiplied by the factor  $\alpha$ , represent the bulk free energy associated with the polar phase expanded up to the fourth order in the polarisation  $\mathbf{P}$ . Here  $\phi_{cr} = \phi_0/2$  is the critical concentration at which the transition from the isotropic (everywhere outside the active drop, where  $|\mathbf{P}| = 0$ ) to the polar phase (only within the active drop where  $|\mathbf{P}| > 0$ ) occurs. The term in gradients of  $\mathbf{P}$  captures the elastic penalty associated local distortions of the polar liquid crystal within the standard approximation of the single elastic constant  $\kappa$  [48]. The penultimate contribution, whose strength is controlled by the coefficients  $\epsilon_{ij}$ , mimics a repulsive effect essentially penalizing the overlap between the active drop and the pillars while the last term, multiplied by the coefficients  $\gamma_{ij}$  and modeling adhesion, favours the contact between them.

In summary, at equilibrium we have the following phases obtained minimizing the free energy  $F = \int_V f dV$ : a passive isotropic fluid (where  $\phi_1 = 0$ ,  $\phi_2 = 0$ ,  $\phi_3 = 0$  and  $\mathbf{P} = 0$ ) external to the active drop and to the pillars; a polarized region (where  $\mathbf{P} = \mathbf{P}_{eq}$ ,  $\phi_1 = \phi_{eq}$ ,  $\phi_2 = 0$ ,  $\phi_3 = 0$ ) located solely within the drop containing the contractile material; two solid pillars (where  $\phi_1 = 0$ ,  $\mathbf{P} = 0$ , with  $\phi_2 = \phi_{eq}$  and  $\phi_3 = 0$  in the pillar at the top while  $\phi_2 = 0$  and  $\phi_3 = \phi_{eq}$  in the one at the bottom). The values of  $\phi_{eq}$  and  $\mathbf{P}_{eq}$  are found by minimizing  $F$  in a state of uniform  $\phi_i$  and  $\mathbf{P}$ . Across the interface of the active droplet, the values of  $\phi_1$  and  $\mathbf{P}$  vary smoothly from  $\phi_1 = \phi_0$  and  $\mathbf{P} = \mathbf{P}_{eq}$  to  $\phi_1 = 0$  and  $\mathbf{P} = 0$ . Finally, we assume equal repulsion between all phase fields, thus  $\epsilon_{ij} = \epsilon$  (with  $\epsilon$  fixed at 0.1), and nonzero equal adhesion only between the drop and the two pillars, hence  $\gamma_{12} = \gamma_{13}$ .

### Equations of motion

On a general basis, the dynamics of the order parameters  $\phi_i$  is governed by a set of Cahn-Hilliard equations

$$\frac{\partial \phi_i}{\partial t} + \nabla \cdot (\phi_i \mathbf{v}) = M \nabla^2 \mu_i, \quad (2)$$

where  $M$  is the mobility and  $\mu_i = \delta F / \delta \phi_i$  is the chemical potential. This is the canonical Model B [67] describing the dynamics of a conserved scalar order parameter  $\phi$ . Note that in our model the evolving phase field is  $\phi_1$  which is associated to the active drop, while the other two,  $\phi_2$  and  $\phi_3$  modeling the pillars, are static. The presence of further active drops (not considered in this paper) would require the inclusion an equivalent number of dynamic phase fields.

The evolution equation for the polarization  $\mathbf{P}(\mathbf{r}, t)$  is given by [1]

$$\frac{\partial \mathbf{P}}{\partial t} + (\mathbf{v} \cdot \nabla) \mathbf{P} = -\underline{\underline{\Omega}} \cdot \mathbf{P} + \xi \underline{\underline{D}} \cdot \mathbf{P} - \frac{1}{\Gamma} \frac{\delta F}{\delta \mathbf{P}}, \quad (3)$$

where  $\underline{\underline{D}} = (\underline{\underline{W}} + \underline{\underline{W}}^T)/2$  and  $\underline{\underline{\Omega}} = (\underline{\underline{W}} - \underline{\underline{W}}^T)/2$  are the symmetric and antisymmetric part of the velocity gradient tensor  $W_{\alpha\beta} = \partial_\beta v_\alpha$ . The constant  $\xi$  depends on the geometry of the active particles, it is positive for the rod-like ones and negative for the oblate ones. In addition, it controls the response of such entities under shear, whether they are flow aligning ( $|\xi| > 1$ ) or flow tumbling ( $|\xi| < 1$ ). In the former case (the one considered in this paper), they align along the flow direction at a fixed angle, whereas in the latter they reorient chaotically. As in previous works [20, 25], we have set  $\xi > 1$ . The last term is the molecular field  $\mathbf{h} = \delta F / \delta \mathbf{P}$ , a quantity governing the relaxation of the liquid crystal towards equilibrium, multiplied by the rotational viscosity  $\Gamma$  which sets the time scale of the relaxation.

The fluid velocity  $\mathbf{v}$  obeys the Navier-Stokes equations which, in the incompressible limit, are

$$\nabla \cdot \mathbf{v} = 0, \quad (4)$$

$$\rho \left( \frac{\partial}{\partial t} + \mathbf{v} \cdot \nabla \right) \mathbf{v} = -\nabla p + \nabla \cdot (\underline{\underline{\sigma}}^{\text{active}} + \underline{\underline{\sigma}}^{\text{passive}}), \quad (5)$$

where  $\rho$  is the density of the fluid and  $p$  is the isotropic pressure. At the right hand side of Equation 5,  $\underline{\underline{\sigma}}^{\text{active}} + \underline{\underline{\sigma}}^{\text{passive}}$  is the total stress tensor, given by the sum of two contributions. The first one is

$$\sigma_{\alpha\beta}^{\text{active}} = -\zeta\phi_1 \left( P_\alpha P_\beta - \frac{1}{d} |\mathbf{P}|^2 \delta_{\alpha\beta} \right), \quad (6)$$

where  $d$  is the dimension of the system and  $\zeta$  is a phenomenological parameter gauging the activity strength, positive for extensile particles and negative for contractile ones [1]. The Greek indexes denote Cartesian components. In our model  $\zeta$  is negative, signifying the tendency of the active gel to contract along the direction of the inner units (e.g. the actin filaments). The functional form of Equation 6 can be derived by summing the contribution of each force dipole (produced using energy coming from, for example, ATP hydrolysis of the myosin) and then coarse graining [4].

The passive stress comprises three contributions, namely a viscous term given by

$$\sigma_{\alpha\beta}^{\text{viscous}} = \eta(\partial_\alpha v_\beta + \partial_\beta v_\alpha) \quad (7)$$

where  $\eta$  is the shear viscosity, summed with an elastic stress  $\underline{\underline{\sigma}}^{\text{elastic}}$ , due to bulk distortions of the liquid crystal, and a surface tension term  $\underline{\underline{\sigma}}^{\text{interface}}$ . The elastic term is

$$\sigma_{\alpha\beta}^{\text{elastic}} = \frac{1}{2}(P_\alpha h_\beta - P_\beta h_\alpha) - \frac{\xi}{2}(P_\alpha h_\beta + P_\beta h_\alpha) - \kappa \partial_\alpha P_\gamma \partial_\beta P_\gamma, \quad (8)$$

while the interfacial one is

$$\sigma_{\alpha\beta}^{\text{interface}} = \sum_i \left[ \left( f - \phi_i \frac{\delta \mathcal{F}}{\delta \phi_i} \right) \delta_{\alpha\beta} - \frac{\partial f}{\partial (\partial_\beta \phi_i)} \partial_\alpha \phi_i \right]. \quad (9)$$

Note that the sum in Equation 9 is necessary since one has to include the contributions due to the pillars, whereas Equation 8 solely accounts for those stemming from the liquid crystal confined within the motile droplet.

Equations 2-3-4-5 are numerically solved by using a hybrid lattice Boltzmann (LB) approach [66, 68], in which a predictor-corrector integration scheme is used for Equations 2 and 3 while a standard LB method is employed for Equations 4 and 5. This method has been successfully tested for a variety of soft matter systems, ranging from binary fluids [69], liquid crystals [70] and active matter [39, 68]. Further details about numerical implementation and thermodynamic parameters can be found in the Supplementary Notes 1 and 2.

## DATA AVAILABILITY

Necessary information to reproduce the simulated data is provided in Methods section and in Supplementary Information. Data are also available upon request from the authors.

## REFERENCES

- [1] M. C. Marchetti, J. F. Joanny, T. Ramaswamy, T. B. Liverpool, J. Prost, M. Rao, and R. Aditi Simha, "Hydrodynamics of soft active matter," *Rev. Mod. Phys.* **85**, 1143 (2013).
- [2] S. Ramaswamy, "The mechanics and statistics of active matter," *Annu. Rev. Cond. Mat. Phys.* **1**, 323–345 (2010).
- [3] J. Prost, F. Jülicher, and J.-F. Joanny, "Active gel physics," *Nature Physics* **11**, 111–117 (2015).
- [4] Y. Hatwalne, S. Ramaswamy, M. Rao, and R. A. Simha, "Rheology of active-particle suspensions," *Phys. Rev. Lett.* **92**, 118101 (2004).
- [5] K. Kruse, J.-F. Joanny, F. Jülicher, J. Prost, and K. Sekimoto, "Asters, vortices, and rotating spirals in active gels of polar filaments," *Phys. Rev. Lett.* **92**, 078101 (2004).
- [6] A. Doostmohammadi, J. Ignés-Mullol, J. M. Yeomans, and F. Sagués, "Active nematics," *Nature Commun.* **9**, 3246 (2018).
- [7] M. Abkenar, K. Marx, T. Auth, and G. Gompper, "Collective behavior of penetrable self-propelled rods in two dimensions," *Phys. Rev. E* **88**, 062314 (2013).
- [8] C. Dombrowski, L. Cisneros, S. Chatkaew, R. E. Goldstein, and J. O. Kessler, "Self-concentration and large-scale coherence in bacterial dynamics," *Phys. Rev. Lett.* **93**, 098103 (2004).
- [9] D. Dell'Arciprete, M. L. Blow, A. T. Brown, F. D. C. Farrell, J. S. Lintuvuori, A. F. McVey, D. Marenduzzo, and W. C. K. Poon, "A growing bacterial colony in two dimensions as an active nematic," *Nature Commun.* **9**, 4190 (2018).
- [10] F. Peruani, A. Deutsch, and M. Bär, "Nonequilibrium clustering of self-propelled rods," *Phys. Rev. E* **74**, 030904(R) (2006).
- [11] F. J. Surrey, T. amd Nédélec, S. Leibler, and E. Karsenti, "Physical properties determining self-organization of motors and microtubules," *Science* **292**, 1167 (2001).
- [12] T. Sanchez, D. T. N. Chen, S. J. DeCamp, M. Heymann, and Z. Dogic, "Spontaneous motion in hierarchically assembled active matter," *Nature* **491**, 431–434 (2012).
- [13] M. S. Silva, M. Depken, B. Stuhmann, M. Korsten, F. C. MacKintosh, and G. H. Koenderink, "Active multistage coarsening of actin networks driven by myosin motors," *Proc. Natl. Acad. Sci. USA* **108**, 9408–9413 (2011).
- [14] V. Schaller, C. Weber, C. Semmrich, E. Frey, and A. R. Bausch, "Polar patterns of driven filaments," *Nature* **467**, 73–77 (2010).
- [15] S. J. DeCamp, G. S. Redner, A. Baskaran, M. F. Hagan, and Z. Dogic, "Orientational order of motile defects in active nematics," *Nature Materials* **14**, 1110–1115 (2015).

- [16] Y. Sumino, K. H. Nagai, Y. Shitaka, K. Yoshikawa, H. Chaté, and K. Oiwa, “Large-scale vortex lattice emerging from collectively moving microtubules,” *Nature* **483**, 448–452 (2012).
- [17] H. H. Wensink, J. Dunkel, S. Heidenreich, K. Drescher, H. Lowen, R. E. Goldstein, and J. M. Yeomans, “Mesoscale turbulence in living fluids,” *Proc. Natl. Acad. Sci. USA* **109**, 14308–14313 (2012).
- [18] H. M. López, J. Gachelin, C. Douarche, H. Auradou, and E. Clément, “Turning bacteria suspensions into superfluids,” *Phys. Rev. Lett.* **115**, 028301 (2015).
- [19] D. Saintillan, “Rheology of active fluids,” *Annu. Rev. Fluid Mech.* **50**, 563–592 (2018).
- [20] E. Tjhung, D. Marenduzzo, and M. E. Cates, “Spontaneous symmetry breaking in active droplets provides a generic route to motility,” *Proc. Nat. Acad. Sci., USA* **109**, 12381–12386 (2012).
- [21] L. Giomi and A. DeSimone, “Spontaneous division and motility in active nematic droplets,” *Phys. Rev. Lett.* **112**, 147802 (2014).
- [22] P. Guillamat, Z. Kos, J. Hardoüin, J. Ignés-Mullol, M. Ravnik, and F. Sagués, “Active nematic emulsions,” *Science Advances* **4**, 4 (2018).
- [23] R. Zhang, Y. Zhou, M. Rahimi, and J. J. de Pablo, “Dynamic structure of active nematic shells,” *Nature* **16**, 3058 (2016).
- [24] F. C. Keber, E. Loiseau, T. Sanchez, S. J. Decamp, L. Giomi, M. J. Bowick, M. C. Marchetti, Z. Dogic, and A. R. Bausch, “Topology and dynamics of active nematic vesicles,” *Science* **345**, 1135–1139 (2014).
- [25] E. Tjhung, A. Tiribocchi, D. Marenduzzo, and M. E. Cates, “A minimal physical model captures the shapes of crawling cells,” *Nature Commun.* **6**, 5420 (2015).
- [26] J. Löber, F. Ziebert, and I. S. Aranson, “Collisions of deformable cells lead to collective migration,” *Sci. Rep.* **5**, 1–7 (2015).
- [27] T. B. Saw, A. Doostmohammadi, V. Nier, L. Kocgozlu, S. Thampi, Y. Toyama, P. Marcq, C. T. Lim, J. M. Yeomans, and B. Ladoux, “Topological defects in epithelia govern cell death and extrusion,” *Nature* **544**, 212–216 (2017).
- [28] C. C. Maass, C. Krüger, S. Herminghaus, and C. Bahr, “Swimming droplets,” *Annu. Rev. Cond. Mat. Phys.* **7**, 171–193 (2015).
- [29] M. Li, M. Brinkmann, I. Pagonabarraga, R. Seemann, and J. P. Fleury, “Spatiotemporal control of cargo delivery performed by programmable self-propelled janus droplets,” *Commun. Phys.* **1**, 23 (2018).
- [30] M. A. Augusting and Y. Hemar, “Nano- and microstructured assemblies for encapsulation of food ingredients,” *Chem. Soc. Rev.* **38**, 902–912 (2009).
- [31] S. H. Au, B. D. Storey, J. C. Moore, Q. Tang, Y.-L. Chen, S. Javaid, A. Fatih Sarioglu, R. Sullivan, M. W. Madden, R. O’Keefe, D. A. Haber, S. Maheswaran, D. M. Langenau, S. L. Stott, and M. Toner, “Clusters of circulating tumor cells traverse capillary-sized vessels,” *Proc. Nat. Acad. Sci. USA* **113**, 4947–4952 (2016).
- [32] B. J. Bentley and L. G. Leal, “An experimental investigation of drop deformation and breakup in steady, two-dimensional linear flows,” *J. Fluid. Mech.* **167**, 241 (1986).
- [33] H. A. Stone, “Dynamics of drop deformation and breakup in viscous fluids,” *Annu. Rev. Fluid Mech.* **26**, 65 (1994).
- [34] F. Jülicher, K. Kruse, J. Prost, and J.-F. Joanny, “Active behavior of the cytoskeleton,” *Physics Reports* **449**, 3–28 (2007).
- [35] D. Shao, H. Levine, and W.-J. Rappel, “Coupling actin flow, adhesion, and morphology in a computational cell motility model,” *Proc. Natl. Acad. Sci. USA* **109**, 6851–6856 (2012).
- [36] B. A. Camley, Y. Zhang, Y. Zhao, B. Li, E. Ben-Jacob, H. Levine, and W.-J. Rappel, “Polarity mechanisms such as contact inhibition of locomotion regulate persistent rotational motion of mammalian cells on micropatterns,” *Proc. Natl. Acad. Sci. USA* **111**, 14770–14775 (2014).
- [37] F. Ziebert and I. S. Aranson, “Computational approaches to substrate-based cell motility,” *npj Comput. Mater.* **2**, 16019 (2016).
- [38] G. De Magistris, A. Tiribocchi, C. A. Whitfield, R. J. Hawkins, D. Marenduzzo, and M. E. Cates, “Spontaneous motility of passive emulsion droplets in polar active gels,” *Soft Matter* **10**, 7826–7837 (2014).
- [39] L. N. Carena, G. Gonnella, D. Marenduzzo, and G. Negro, “Rotation and propulsion in 3d active chiral droplets,” *Proc. Natl. Acad. Sci., USA* **116**, 22065–22070 (2019).
- [40] F. Ziebert, S. Swaminathan, and I. S. Aranson, “Model for self-polarization and motility of keratocyte fragments,” *J. R. Soc. Interface* **9**, 1084–1092 (2012).
- [41] F. Ziebert and I. S. Aranson, “Effects of adhesion dynamics and substrate compliance on the shape and motility of crawling cells,” *Plos One* **9**, 1084–1092 (2013).
- [42] B. Winkler, I. S. Aranson, and F. Ziebert, “Membrane tension feedback on shape and motility of eukaryotic cells,” *Physica D* **318**, 26–33 (2016).
- [43] W. Marth and A. Voigt, “Collective migration under hydrodynamic interactions: a computational approach,” *Interface Focus* **6**, 20160037 (2016).
- [44] P. M. Davidson, J. Sliz, P. Isermann, C. Denais, and J. Lammerding, “Design of a microfluidic device to quantify dynamic intra-nuclear deformation during cell migration through confining environments,” *Integrative Biology* **7**, 1534–1546 (2015).
- [45] X. Cao, E. Moeendarbary, P. Isermann, P. M. Davidson, X. Wang, M. B. Chen, A. K. Burkart, J. Lammerding, R. D. Kamm, and V. B. Shenoy, “A chemomechanical model for nuclear morphology and stresses during cell transendothelial migration,” *Biophysical Journal* **111**, 1541–1552 (2016).
- [46] D. B. Brückner, A. Fink, C. Schreiber, P. J. Röttgermann, J. O. Rädler, and C. P. Broedersz, “Stochastic nonlinear dynamics of confined cell migration in two-state systems,” *Nature Physics* **15**, 595–601 (2019).
- [47] S. R. De Groot and P. Mazur, *Non-equilibrium thermodynamics* (Dover Publications, 1984).
- [48] P. G. de Gennes and J. Prost, *The physics of liquid crystals* (Oxford University Press, 2nd ed., 1993).
- [49] C. A. Whitfield, D. Marenduzzo, R. Voituriez, and R. J. Hawkins, “Active polar fluid flow in finite droplets,” *Eur. Phys. Jour. E* **37**, 8 (2014).
- [50] M. L. Blow, S. Thampi, and J. M. Yeomans, “Biphasic, lyotropic, active nematics,” *Phys. Rev. Lett.* **248303**, 2014 (113).
- [51] R. Poincloux, O. Collin, F. Lizárraga, M. Romao, M. Debray, M. Piel, and P. Chavrier, “Contractility of the cell rear drives invasion of breast tumor cells in 3d matrigel,” *Proc. Natl. Acad. Sci. USA* **108**, 1943–1948 (2011).

- [52] D. Bray, *Cell Movements: From Molecules to Motility* (Garland Science, 2000).
- [53] U. S. Schwarz and S. A. Safran, “Physics of adherent cells,” *Rev. Mod. Phys.* **85**, 1327 (2013).
- [54] U. Euteneuer and M. Schliwa, “Persistent, directional motility of cells and cytoplasmic fragments in the absence of microtubules,” *Nature* **310**, 58 (1984).
- [55] C. Blanch-Mercader and J. Casademunt, “Spontaneous motility of actin lamellar fragments,” *Phys. Rev. Lett.* **110**, 078102 (2013).
- [56] T. F. Didar and M. Tabrizian, “Adhesion based detection, sorting and enrichment of cells in microfluidic lab-on-chip devices,” *Lab on a Chip* **10**, 3043–3053 (2010).
- [57] K. M. Stroka, H. Jiang, S. H. Chen, Z. Tong, D. Wirtz, S. X. Sun, and K. Konstantopoulos, “Water permeation drives tumor cell migration in confined microenvironments,” *Cell* **157**, 611–623 (2014).
- [58] D. K. Lubensky and D. R. Nelson, “Driven polymer translocation through a narrow pore,” *Biophys. J.* **77**, 1824–1838 (1999).
- [59] H. W. Hou, Q. S. Li, G. Y. H. Lee, A. P. Kumar, C. N. Ong, and C. T. Lim, “Deformability study of breast cancer cells using microfluidics,” *Biomedical Microdevices* **11**, 557–564 (2009).
- [60] A. Raj and A. K. Sen, “Entry and passage behavior of biological cells in a constricted compliant microchannel,” *RSC Advances* **8**, 20884–20893 (2018).
- [61] P. M. Davidson, A. Battistella, T. Déjardin, T. Betz, J. Plastino, N. Borghi, B. Cadot, and C. Sykes, “Nesprin-2 accumulates at the front of the nucleus during confined cell migration,” *Embo Reports* **21**, e49910 (2020).
- [62] A. Tiribocchi, A. Montessori, M. Lauricella, F. Bonaccorso, S. Succi, S. Aime, M. Milani, and D. Weitz, “The vortex-drive dynamics of droplets within droplets,” *Nature Commun.* **12**, 82 (2021).
- [63] M. Paoluzzi, R. Di Leonardo, M. C. Marchetti, and L. Angelani, “Shape and displacement fluctuations in soft vesicles filled by active particles,” *Sci. Rep.* **6**, 34146 (2006).
- [64] H. R. Vutukuri, M. Hoore, C. Abaurrea-Velasco, L. van Buren, A. Dutto, T. Auth, D. A. Fedosov, G. Gompper, and J. Vermant, “Active particles induce large shape deformations in giant lipid vesicles,” *Nature* **586**, 52–56 (2020).
- [65] M. S. E. Peterson, A. Baskaran, and M. F. Hagan, “Vesicle shape transformations driven by confined active filaments,” *Nature Commun.* **12**, 7247 (2021).
- [66] S. Succi, “The lattice boltzmann equation: For complex states of flowing matter,” Oxford University Press (2018).
- [67] A. J. Bray, “Theory of phase-ordering kinetics,” *Advances in Physics* **43**, 357–459 (1994).
- [68] L. N. Carenza, G. Gonnella, A. Lamura, G. Negro, and A. Tiribocchi, “Lattice boltzmann methods and active fluids,” *Eur. Phys. Jour. E* **42**, 81 (2019).
- [69] M. R. Swift, E. Orlandini, W. R. Osborn, and J. M. Yeomans, “Lattice boltzmann simulations of liquid-gas and binary fluid systems,” *Phys. Rev. E* **54**, 5041 (1996).
- [70] M. E. Cates, O. Henrich, D. Marenduzzo, and K. Stratford, “Lattice boltzmann simulations of liquid crystalline fluids: active gels and blue phases,” *Soft Matter* **5**, 3791–3800 (2009).

## ACKNOWLEDGMENTS

A. T., M. D., M. L., A. M. and S. S. acknowledge funding from the European Research Council under the European Union’s Horizon 2020 Framework Programme (No. FP/2014-2020) ERC Grant Agreement No.739964 (COPMAT) and ERC-PoC2 grant No. 101081171 (Drop-Track). A. T. and D. M. warmly thank Antonio Basoni, Giuseppe Gonnella and Alexander Morozov for useful discussions.

## AUTHOR CONTRIBUTIONS

A. T. conceived the project. A. T. and S. S. designed the research with the support of M. D., M. L. and A. M.. A.T. run simulations and processed data. A.T. analyzed the results with M. D., M. L., A. M., D. M. and S.S. The paper is written by A. T. with contributions from M. D., M. L., A. M., D. M. and S.S.

## COMPETING INTERESTS

The authors declare no competing interests.



## SUPPLEMENTARY NOTE 1: NUMERICAL ASPECTS

In this section we provide further details about the computational model and the simulation parameters.

The equation of the order parameter  $\phi_1$  (Equation 2 of the main text), the one of the polarization  $\mathbf{P}$  (Equation 3 of the main text) and the Navier-Stokes equations (Equations 4 and 5 of the main text) are integrated by using a hybrid lattice Boltzmann (LB) method [68], where the first two are solved via a finite-difference predictor-corrector scheme and the latter through a standard LB approach.

Simulations are run on rectangular boxes, where the vertical direction is kept constant at  $L_z = 170$  while the horizontal one  $L_y$  ranges between 500 and 700 lattice sites. We set periodic boundary conditions along the  $y$ -axis and two flat walls along the  $z$ -axis, placed at  $z = 0$  and  $z = L_z$ . Within the microchannel we place a droplet containing an active gel, whose concentration is described by the scalar field  $\phi_1(\mathbf{r}, t)$ , kept approximately equal to 2 inside and 0 everywhere else, and whose orientation is captured by the polar field  $\mathbf{P}(\mathbf{r}, t)$ , initially uniform and parallel to the  $y$  direction within the drop ( $\mathbf{P}(\mathbf{r}, 0) = \mathbf{P}_y(\mathbf{r}, 0)$ , with  $|\mathbf{P}_y| = 1$ ) and zero outside. At the walls of the channel we impose no-slip conditions for the velocity field, i.e.  $v|_{z=0, L_z} = 0$ , and no wetting for  $\phi_1$ , i.e.  $\phi_1|_{z=0, L_z} = 0$  throughout the simulation. No specific anchoring conditions (such as perpendicular or parallel) are imposed at the walls for the polar field  $\mathbf{P}$ .

Following the design proposed in Ref.[44], the constriction is represented by two semi-circular pillars placed symmetrically at distance  $h$  and attached to opposite walls (see Fig.2 of the main text). Their solid structure is modeled through two auxiliary *static* phase fields  $\phi_2(\mathbf{r})$  and  $\phi_3(\mathbf{r})$ , positive within each pillar and zero outside. In addition, the velocity field is set to zero inside throughout the simulation. Finally, to ensure that their interface remains perpendicular to the flat walls, we impose neutral wetting condition for both phase fields. Although a more accurate modeling of the constriction is possible (using, for example, a full lattice Boltzmann approach [1, 68]), this one combines a good numerical stability with a relatively easy implementation of mesoscale interactions (such as repulsion and adhesion controlled by proper free energy terms, see Eq.1 of the main text) between the active droplet and the pore.

Thermodynamic parameters have been chosen as follows:  $a = 0.04$ ,  $k = 0.06$ ,  $M = 0.1$ ,  $\alpha = 0.1$ ,  $\kappa = 0.04$ ,  $\xi = 1.1$ ,  $\Gamma = 1$ ,  $\eta \simeq 1.67$ ,  $\epsilon_{ij, i < j} = \epsilon = 0.1$ . Their choice generally ensures a high numerical stability and a reasonable mapping to real physical units (see next section). In particular, the first two values,  $a$  and  $k$ , control the surface tension  $\sigma$  of the active droplet, given by  $\sigma = \sqrt{8ak/9} \simeq 0.045$ , while  $\alpha$  fixes the values of  $\phi_{\text{eq}}$  and  $\mathbf{P}_{\text{eq}}$  (see section Methods of the main text) and controls

the isotropic-to-polar transition. Also,  $\kappa$  and  $\xi$  describe the elasticity of the polar liquid crystal, with the latter larger than 1 to account for flow aligning particles. The rotational viscosity  $\Gamma$  sets the time scale of the relaxation of the polarization and describes the viscous torque associated with its rotation, while  $\eta$  represents the viscosity of fluid, both within and outside the droplet. Finally, an equal repulsion, whose strength is controlled by  $\epsilon$ , is set between droplet and pillars. Its value is high enough to prevent merging between different phase fields.

Lattice spacing and integration timestep are kept fixed to  $\Delta x = 1$  and  $\Delta t = 1$ . The contractile activity  $\zeta$  has been varied between  $-10^{-4}$  and  $-10^{-3}$ . Keeping fixed the thermodynamic parameters defined above, the optimal values of  $\zeta$  ensuring a balance between interfacial deformations and splay distortions (guaranteeing a rectilinear motion) range roughly between  $-5 \times 10^{-4}$  and  $-10^{-3}$ . Finally, the constant  $\gamma_{ij}$  in Eq.1 of the main text gauges the strength of the adhesion forces. We impose an equal value of adhesion coefficient between drop and each pillars, i.e.  $\gamma_{12} = \gamma_{13}$ , while other entries are set to zero. Since a constant value of  $\gamma$  throughout the pore generally does not yield a complete crossing, we set two different values  $\gamma_L$  and  $\gamma_R$  of adhesiveness on the half left of the pore (entry) and on the half right (exit) respectively, with  $\gamma_L > \gamma_R$ , to ensure a transmigration along the positive direction of the  $y$ -axis. In our simulations they approximately vary between  $10^{-3}$  and  $5 \times 10^{-2}$ , while optimal values generally depend on the previous thermodynamic parameters as well as on the ratio  $\lambda = h/D$ , where  $D$  is the diameter of the droplet. As discussed in the main text,  $\lambda$  ranges from 0.2 to 0.8.

## SUPPLEMENTARY NOTE 2: MAPPING TO PHYSICAL UNITS

Here we provide an approximate mapping between simulation parameters and real physical units. Our runs are performed on a rectangular mesh of size varying from  $L_y = 500 \div 700$  (length of the channel) to  $L_z = 170$  (height of the channel), with lattice spacing  $\Delta x = 1$  and integration time step  $\Delta t = 1$ . A droplet of radius  $R = 45$  lattice sites is placed within the microchannel, sufficiently far away from the constriction. Following previous works on self-propelled active fluid droplets [20, 25], we fix the length, time and force scales to the following values:  $L = 1\mu\text{m}$ ,  $T = 10\text{ms}$  and  $F = 100\text{nN}$  (in simulation units these scales are all equal to one). Hence, our simulation would approximately correspond to a microfluidic channel of length ranging from 0.5 to 1mm in which an active droplet of diameter  $D \simeq 90\mu\text{m}$  has an effective shear viscosity  $\eta_{\text{eff}} \simeq 1.5\text{kPa}\cdot\text{s}$ , an effective elastic constant  $\kappa \simeq 4\text{nN}$ , a surface tension  $\sigma \simeq 4\text{mN/m}$ , moving with speed  $1 \div 10 \mu\text{m/s}$  in a Newtonian fluid, such as water. Also, one would have a rotational viscosity  $\Gamma \simeq 1\text{kPa}\cdot\text{s}$ , a

diffusion coefficient  $D_\phi = Ma \simeq 0.4 \mu\text{m}^2/\text{s}$  and an activity  $\xi \simeq 100\text{Pa}$ . Finally, the drop speed in simulation units varies between  $v \simeq 10^{-4}$  and  $v \simeq 10^{-3}$ , values that keep the Reynolds number  $\text{Re} = v\rho D/\eta$  lower than 0.1 and ensure that inertial effects can be neglected. In addition, the capillary number  $\text{Ca} = v\eta/\sigma$  ranges approximately between 0.1 and 0.001, thus droplet rupture remains an unlikely event.

### SUPPLEMENTARY NOTE 3: SUPPRESSION OF TRANSMIGRATION IN THE PRESENCE OF ADHESION

As discussed in the main text, the transmigration through sufficiently narrow constrictions is generally inhibited if a constant and uniform value of  $\gamma$  is set between droplet and pillars. In Fig.2 of the main text we have shown that the process can actually occur if the adhesion coefficient at the entry of the pore,  $\gamma_L$ , is larger than the one the exit,  $\gamma_R$ , provided that  $\gamma_{\min,L} \leq \gamma_L \leq \gamma_{\max,L}$  and  $\gamma_{\min,R} \leq \gamma_R \leq \gamma_{\max,R}$ .

In Supplementary Movie 7 we show an active droplet moving within a microchannel where  $\lambda \simeq 0.5$ ,  $\gamma_L = 5 \times 10^{-2}$  and  $\gamma_R = 3 \times 10^{-2}$ . Note that, with this value of  $\lambda$ , one has  $\gamma_{\min,L} \simeq 2 \times 10^{-2}$ ,  $\gamma_{\max,L} \simeq 5 \times 10^{-2}$ ,  $\gamma_{\min,R} \simeq 5 \times 10^{-3}$  and  $\gamma_{\max,R} \simeq 2 \times 10^{-2}$ , thus the transmigration is expected to be suppressed, since  $\gamma_R > \gamma_{\max,R}$ . At the entry of the pore the dynamics is overall akin to that discussed in Fig.2 of the main text for  $\lambda \simeq 0.5$ . Indeed, portions of the interface, approximately located on opposite sides with respect to the longitudinal midline of the microchannel, adhere to the pillars, enabling the droplet to squeeze in. However, once a large part (more than half) of the droplet has passed the center of the pore, the motion stops and the droplet gets stuck on a peanutlike configuration. This occurs because the droplet propulsion is not sufficient to overcome the excess of adhesion (controlled by  $\gamma_R$ ) which, increasing the connectivity between interface and pillars, ultimately prevents the transmigration.

In Supplementary Movie 8 we show the case in which  $\lambda \simeq 0.2$ ,  $\gamma_L = 1.5 \times 10^{-2}$  and  $\gamma_R = 10^{-2}$ . Here  $\gamma_{\min,L} \simeq 2 \times 10^{-2}$ ,  $\gamma_{\max,L} \simeq 4 \times 10^{-2}$ ,  $\gamma_{\min,R} \simeq 5 \times 10^{-3}$ ,  $\gamma_{\max,R} \simeq 1.5 \times 10^{-2}$ , hence once again the crossing should be inhibited since  $\gamma_L < \gamma_{\min,L}$ . Indeed, once the droplet hits the pore, the low adhesion forces at the entry (controlled by  $\gamma_L$ ) do not guarantee a prolonged contact between interface and pillars, thus basically impeding the droplet to snake in. The rearrangement of the liquid crystal orientation due to the internal fluid flow drives the droplet downwards and then backwards, causing its detachment from the pore.

As mentioned in the main text we note that the values of the adhesion coefficients depend upon other thermodynamic parameters, such as elasticity of the liquid crystal

and interfacial tension, speed of the droplet, viscosity, diffusion constant, repulsion as well as initial position, whose modification would require an adjustment of  $\gamma_L$  and  $\gamma_R$ .

### SUPPLEMENTARY NOTE 4: SMOOTHER ADHESION DESIGN

In the main text we have shown that the transmigration occurs if two different adhesion coefficients,  $\gamma_L$  and  $\gamma_R$ , are set at the entry and exit of the gap, with  $\gamma_L > \gamma_R$ . More specifically, if the diameter of the pillar is  $l$ , one has  $\gamma = \gamma_L$  for  $0 \leq y \leq l/2$  and  $\gamma = \gamma_R$  for  $l/2 \leq y \leq l$ , i.e. the adhesion strength changes sharply following a step function. A smoother variation can be obtained by assuming that  $\gamma(y) = 0.5[(\gamma_L + \gamma_R) + (\gamma_L - \gamma_R) \tanh((-y + y_0)/a)]$ , where  $y_0$  and  $a$  are two constants controlling position and width of the slope around the midline of the constriction. Increasing  $a$  progressively augments the width of  $\gamma(y)$ , thus ultimately diminishing the value of  $\gamma$  nearby the midline of the pillars (see Fig.8). In Supplementary Movie 9 we show, for example, three simulations for  $\lambda \simeq 0.5$  and  $a = 1$  (left),  $a = 15$  (middle),  $a = 20$  (right), while other parameters are kept equal to those of Fig.2g-n of the main text. Our results show that the typical dynamic features of a droplet crossing a medium-size constriction are preserved albeit, for increasing values of  $a$ , the transmigration time gradually augments (see Fig.9) until the process is completely arrested and the drop gets trapped within the pore.

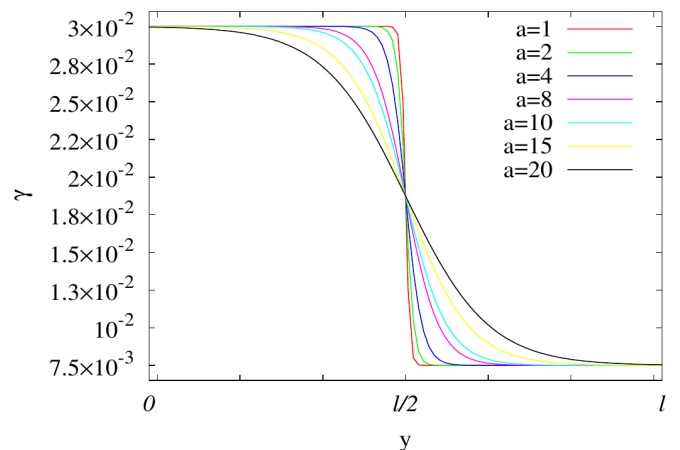


Figure 8. Functional forms of the adhesion strength within the constriction for  $\lambda \simeq 0.5$ . Here  $\gamma(y) = 0.5[(\gamma_L + \gamma_R) + (\gamma_L - \gamma_R) \tanh((-y + y_0)/a)]$ , where  $\gamma_L = 3 \times 10^{-2}$  and  $\gamma_R = 7.5 \times 10^{-3}$ , while  $y_0$  and  $a$  control position and width of the slope. Also,  $l$  is the diameter of the circular pillar. Increasing the parameter  $a$  augments the width of the curve around the midline of the pillars.

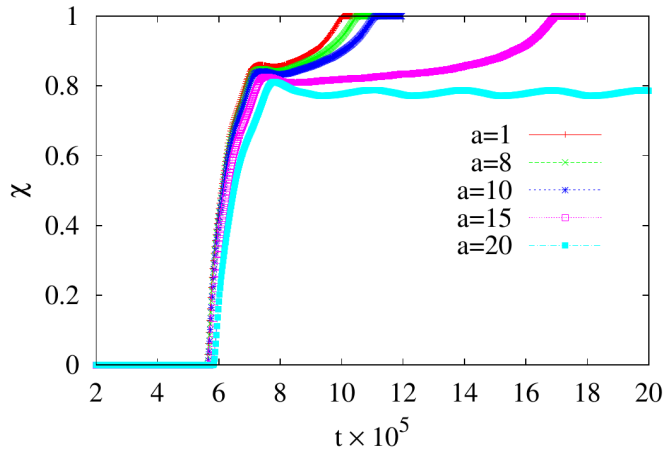


Figure 9. Transmigration order parameter  $\chi(t) = A_C(t)/A_T(t)$  for  $\lambda \simeq 0.5$  and  $a$  ranging from 1 to 20. Other parameters are the same as the ones of Fig.2g-n of the main text. Here  $A_C$  is the area fraction of the droplet between the midline (located at  $l/2$ ) and the exit of the constriction (located at  $l$ ), while  $A_T$  is the total area of the droplet within the pore.

#### SUPPLEMENTARY NOTE 5: THIN FILM-LIKE DYNAMICS

When moving through highly constrained micro-environments, droplets (or cells) can often experience a momentum sink due to the presence of walls placed at very close distance. To account, in a phenomenological

way, for this thin film-like dynamics, one can add, to the momentum balance equation, a frictional force of the form  $\mathbf{f} = -b\mathbf{v}$ , where  $b$  is a frictional coefficient and  $\mathbf{v}$  is the fluid velocity. This approach is often followed in active gel theory to study systems where the dry limit is of experimental relevance, such as in cells crawling on solid substrates [20]. The effect of this extra term leads to results in qualitative agreements with the ones described in the main text. Indeed, although the frictional force reduces the droplet speed, the crossing is generally guaranteed unless  $b$  overcomes a critical drag  $b_c$  (whose value depends on the other model parameters) beyond which the transmigration is hindered. In Supplementary Movie 10 we show, for example, two simulations for  $\lambda \simeq 0.5$  with  $b = 5 \times 10^{-4}$  (left) and  $b = 10^{-3}$  (right). Other parameters are the same as those in Fig.2g-n of the main text. While for  $b = 5 \times 10^{-4}$  the transmigration shares the same features as those observed in medium size pores, for  $b > b_c \simeq 10^{-3}$  the drop gets stuck within the pore, since the speed decrease reduces the propulsion necessary to complete the crossing.

#### SUPPLEMENTARY REFERENCES

- 
- [1] T. Krüger, H. Kusumaatmaja, A. Kuzmin, O. Shardt, G. Silva, E.M. Vigen, *The Lattice Boltzmann Method: Principles and Practice*, Springer International Publishing, (2016).